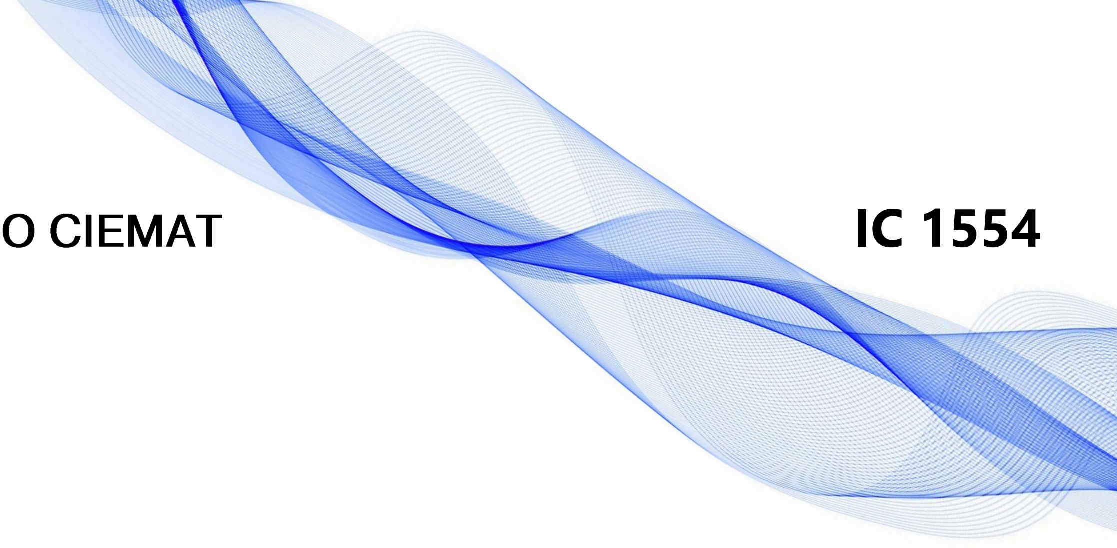

INFORME TÉCNICO CIEMAT

IC 1554

SATURATION OF A BINARY BARRIER (BLOCK /PELLETS) OF MX-80 BENTONITE

Villar Galicia, Mª.V.

Iglesias Martínez, R.J.

García Herrera, G.

Gimeno Labajos, N.

GOBIERNO DE ESPAÑA
MINISTERIO DE CIENCIA, INNOVACIÓN Y UNIVERSIDADES

Ciemat
Centro de Investigaciones Energéticas, Medioambientales y Tecnológicas

Publication available in catalog of official publications

ISSN: 2695-8864
NIPO: 152-25-013-6

Edition and Publication:
Editorial CIEMAT
Avda. Complutense, 40 28040-MADRID
e-mail: editorial@ciemat.es
Editorial news

TABLE OF CONTENTS

LIST OF FIGURES

LIST OF TABLE

1 INTRODUCTION

The sealing ability is a key safety function for bentonite-based barriers in all geological nuclear waste repository concepts. Sealing is achieved by the combination of a high swelling potential and a low hydraulic conductivity. The barriers will be installed as blocks, pellets, and/or granules, which may give place to significant initial heterogeneities. Although the bentonite buffer shows a natural tendency towards homogenisation, long-term observations both in large-scale and in laboratory tests revealed that a degree of heterogeneity may persist in barrier materials even after full saturation (e.g. García-Siñeriz et al. 2015, Villar et al. 2020, Bernachy-Barbe et al. 2020, Bernachy-Barbe 2021). Hence, the effect of heterogeneity on the safety functions of the barrier after saturation needs to be considered (e.g. advection in the barrier) to improve the design and installation of the barrier components. These issues were tackled in the BEACON project whose aim was to evaluate the consequences of heterogeneities on the performance of bentonite barriers in geological repositories for high-level radioactive waste, and to develop, test and improve models able to predict the mechanical evolution of installed bentonite components.

Among the work undertaken in the project, CIEMAT performed a laboratory experimental investigation about the behaviour upon hydration under isochoric conditions of binary samples, i.e. samples composed of a block and a mixture of pellets. It is expected that the combined use of a pellets/powder mixture and a compacted block would give place to more heterogeneous density and stress fields, as was demonstrated in the tests by Martikainen et al. 2018 (reported in Talandier, 2019), where binary samples of MX-80 bentonite were saturated under constant volume. It was the aim of the experiments performed by CIEMAT and reported here to shed light on the stress development upon saturation of a two-part sample of Wyoming bentonite (predominantly sodic). In particular, the block and the pellets/powder mixture had the same initial dry density (1.5 g/cm^3) and regular-shaped pellets (ϕ=7 mm) were used, mixed in a 70/30 mass ratio with bentonite powder.

This kind of pellets and their mixtures with powder were thoroughly characterised in Molinero (2018) and later used in hydration tests by e.g. Darder et al. (2022). They were manufactured from the same material (brand name Laviosa-MPC WH2) as those used in the Full-Scale Seal test (FSS) run by the French nuclear waste agency (ANDRA). This large-scale test aimed to simulate in a surface facility a seal for repositories (Bosgiraud and Foin 2016). In the French repository concept (Cigéo, ANDRA 2013), seals are defined as hydraulic components for closure of large diameter (several meters) underground installations and infrastructure components such as shafts, ramps, drifts and intermediate level waste disposal vaults. Each seal consists of a swelling clay core (SCC) and concrete containment walls. As SCC, mixtures of 32-mm diameter bentonite pellets and powder were tested and used in the FSS test. At a smaller scale, the complementary REM laboratory test reproduced the same seal concept using the same material as in FSS (Conil et al. 2015). In both cases the SCC consisted of alternating layers of pellets (ϕ=32 mm) and crushed bentonite (powder) in the mass proportions of 70/30 with a final dry density of 1.50 g/cm^3. The behaviour upon hydration of this mixture was analysed at the laboratory scale in Bernachy-Barbe et al. (2020).

In the two tests performed by CIEMAT, CT31 and CT32, the testing cell allowed measurement of relative humidity and radial pressures at several locations along the sample. The tests were performed in an instrumented cell (15x15 cm) with MX-80 bentonite. Hydration with deionised water under a low water injection pressure took place through the bottom of the cell, where the mixture part was placed in one of the tests (test CT31) and the block in the other one (test CT32). In all other respects the tests were similar. The tests were dismantled after having reached relative humidity and pressure stabilisation and full saturation. The results of the first test were reported in Villar et al. (2024), and the second related one and the comparison between both constitute the contents of this report.

2 EXPERIMENTAL SETUP

The test setup consists of an instrumented stainless steel cylindrical cell, the hydration system and the control and data acquisition systems (Figure 1).

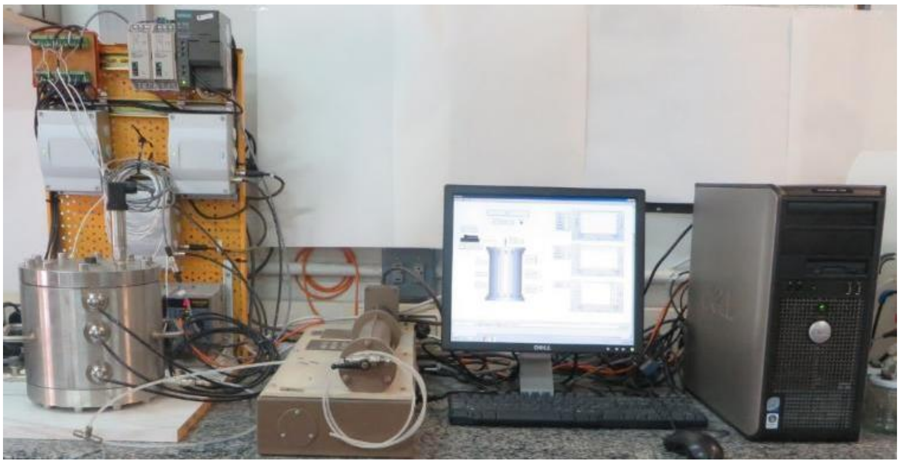

Figure 1. General setup view

A stainless steel cell was used to contain the bentonite. The internal dimensions were 15 cm of diameter and 14.5 cm of height. Figure 2 shows a blueprint of the cell and a photo of its inside, in which the location of sensor is indicated. The cell was instrumented with capacitive-type sensors placed inside the clay at three different levels (13, 78 and 128 mm from the bottom porous stone). The transmitters used were VAISALA HMT337, which include a humidity sensor that changes its dielectrical characteristics with extremely small variations in humidity (capacitive-type RH sensor). They also include a temperature sensing element (Pt 100). The accuracy of the humidity sensor is ±1 % over the range 0-90 percent RH and ±2 % over the range 90-100 percent RH. The sensors were protected by cylindrical stainless steel filters (length 41.5 mm). Radial pressures on the lateral surface of the cell were measured at the same distances from the bottom plate as those for the RH/T transmitters. The pressure sensors used were XPM10, with range 0-100 bar and an error of 0.5 bar. The pore pressure was measured on top of the cell with a PMP 4070 Druck Amplified Output Pressure Transducer with operating absolute pressure range of 0.7-7 bar. Data acquisition of the instrumentation signals was done with a MX100 Yokogawa connected to a control computer. LabVIEW was used to develop the data acquisition application.

The sample was hydrated through a porous stone at the bottom of the cell. Hydration took place with deionised and degassed water injected at a constant pressure of 0.014 MPa by a GDS pressure/volume controller connected to the control computer.

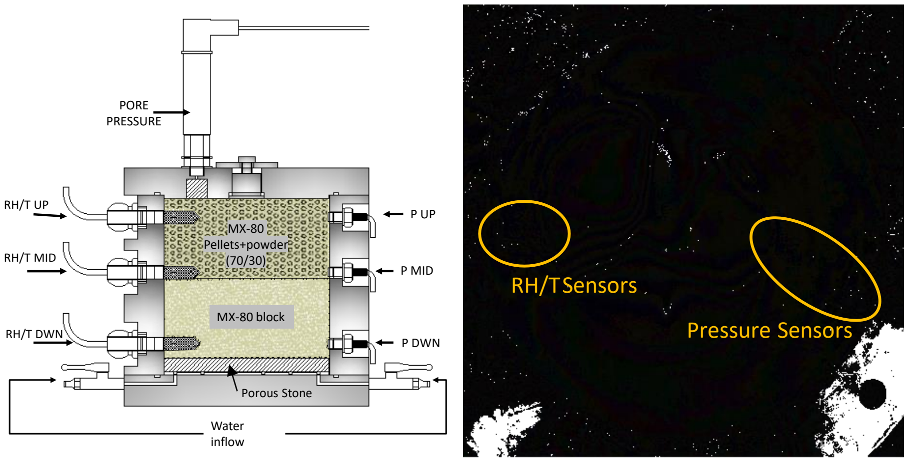

Figure 2. Longitudinal cross-section of the cell with the sensors installed (RH/T: relative humidity and temperature; P: radial pressure, pore pressure sensor on top)

More details about the experimental setup and sensors’ characteristics are given in Villar et al. (2024).

3 MATERIALS

The test was performed with an MX-80 bentonite block and a mixture of bentonite pellets and powder in a mass ratio 70/30. The block was obtained by powder compaction, and the same powder was used in the pellets/powder mixture. The initial water content of the bentonite powder was 8.2 % and of the pellets 7.2 %. The powder had a grain size between 0.1 and 0.75 mm. The pellets had a regular, approximately spherical shape with a diameter of 7 mm and a dry density of 2.0 g/cm^3. They were provided by AITEMIN in 2013 (in turn supplied by Laviosa MPC) in the framework of the in situ test NSC, performed at the Bure URL in France. They were manufactured from the material with brand name WH2 (a Wyoming-type bentonite), but no detailed mineralogical characterisation of the pellets was provided by the suppliers nor performed at CIEMAT. The manufacturer of the pellets (Laviosa MPC) provided a mineralogical composition of 80 % montmorillonite, 8 % anorthite, 4 % quartz, 4 % muscovite and 2 % pyrite (Molinero-Guerra, 2018). Bosgiraud and Foin (2016) characterised the 7-mm diameter pellets, and found for them a dry density of 2.00 g/cm^3, a water content of 4.9 % and a particle density of 2.78 g/cm^3 for the material from which they were produced. The density of solid particles obtained at CIEMAT for the pellets was 2.75 g/cm^3.

The MX-80 bentonite is a brand name used by the American Colloid Company for sodium bentonite from Wyoming (USA), milled to millimetre-sized grains. According to studies performed in different batches of this bentonite by different authors, the content of montmorillonite can be between 65 and 90 %, with quartz, plagioclase and K-feldspars (contents between 4 and 15 %), and minor quantities of cristobalite, tridymite, calcite, gypsum, pyrite and illite. The cation exchange capacity (CEC) is 75-82 meq/100 g, Na^+ is the main exchangeable cation (50-74 meq/100 g), with also Ca^{2+} (10-30 meq/100 g) and Mg^{2+} (3-8 meq/100 g). The main soluble ions are sodium and sulphate.

In the batch of MX-80 used to compact the block and for the powder in the mixture, the smectite content was 92 %, the feldspars content 5 % and the quartz content 1 %, with traces of calcite, gypsum, dolomite, halite and pyrite (Gómez-Espina and Villar 2016). The particle density was 2.78 g/cm^3.

A specific geochemical characterisation was performed for the two raw materials used in this test (pellets and powder). The concentration of ions measured in aqueous extracts of solid:liquid ratio 1:8 is shown in Table 1. Table 2 shows the cations extracted using a solution 0.5 M of $CsNO_3$ at pH 8.2 and the CEC of the raw samples. Since the methodology followed for the extraction of exchangeable cations did not involve previous washing of the samples, both exchangeable and soluble cations were actually measured in the extracts prepared. For this reason the values given correspond in fact to “extractable” cations, in the sense that they may include soluble cations in addition to the exchangeable ones. As well, during the preparation of the extracts, some species could be dissolved and the cations released could enter the exchangeable complex, substituting for other cations. This could be particularly the case of calcium coming from sulphates substituting for sodium. All the values given in these Tables are the average of two measurements.

Reference	**pH**	**Alkalinity**	**Ca^{2+}**	**Na^{+}**	**K^{+}**	**Cl^{-}**	**$SO4^{2-}$**	**HCO^{3-}**
Powder	8.4	5.2	0.2	16.2	0.2	0.2	10.1	5.2
Pellets	8.8	6.0	0.1	13.3	0.2	0.2	6.7	6.0

Table 1. Analysis of the 1:8 aqueous extracts of the raw bentonite materials (meq/L)

Reference	**Na^{+}**	**K^{+}**	**Mg^{2+}**	**Ca^{2+}**	**Sr^{2+}**	**Σ extract.**	**CEC**
Powder	63	1.9	6	20	0.2	91	77
Pellets	61	2.0	5	18	0.1	86	71

Table 2. Extractable cations and CEC of the raw bentonite materials (meq/100 g)

The swelling pressure of small samples (3.8 or 5.0 cm in diameter, 1.2 cm in height) of MX-80 bentonite powder compacted with its hygroscopic water content was determined at CIEMAT at room temperature using deionised water as saturation fluid in standard oedometers. The swelling pressure (P_s, MPa) could be related to the final dry density of the sample (ρ_d, g/cm^3) through the following equation (Villar et al. 2022):

$$\ln P_s = 5.44\ \rho_d - 6.94 \qquad \text{Eq.1}$$

The hydraulic conductivity (k_w, m/s) of samples of powdered MX-80 bentonite (grain size <1 mm), compacted at different dry densities (ρ_d, g/cm^3) and kept in stainless steel cells which hindered the swelling of the material upon saturation, was measured in a constant head permeameter (Villar 2005). Deionised water was used as permeant. The following exponential relation between dry density (ρ_d, g/cm^3) and hydraulic conductivity (k_w, m/s) was found:

$$\log k_w = -2.94\ \rho_d - 8.17 \qquad \text{Eq.2}$$

4 SAMPLE PREPARATION

Test CT32 was performed with the bentonite compacted block in the bottom part of the cell and the pellets/powder mixture in the upper part (Figure 2). The block was compacted at a dry density of 1.50 g/cm^3 inside the cell body using a uniaxial pressure of 10.9 MPa. Then the other half of the cell was filled with the mixture of pellets and MX-80 powder. This mixture was arranged in 8 layers in such a way that the powder filled the gaps between the pellets. Each layer consisted of a first level with 1/3 of powder (~26 g), a second level with the pellets (~180 g), and a third level with the remaining 2/3 of powder (~52 g). During the process, light blows were given to the cell to readjust the particles so that the mass necessary to reach the target dry density of 1.50 g/cm^3 could fit inside. Once a layer was completed, a light pressure was applied to the mixture surface using a circular plate of the same diameter as the cell, so that to get an even layer surface. A total of 1,442 g of pellets (1,351 g dry mass) and 627 g of powder (579 g dry mass) were used for the mixture part. Considering the dry density of the pellets (2.0 g/cm^3), a 56 % of the volume in the GBM corresponded initially to pellets. The middle and upper RH/T sensors were inserted as the cell was being filled (Figure 3, left and middle).

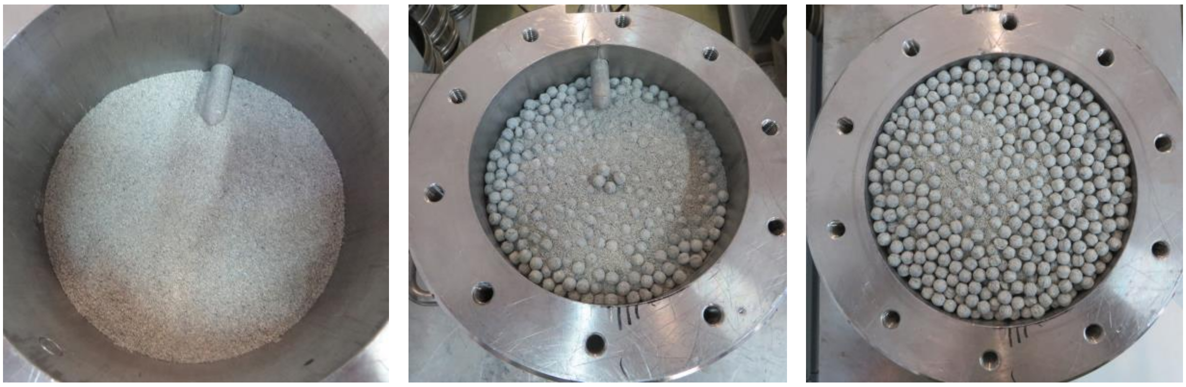

Figure 3. Preparation of the block (left) and pellets/powder mixture halves of the sample (centre and right). The middle photo shows the middle RH/T sensor in place

The initial characteristics of the material inside the cell, including water content (w), dry density (ρ_d), degree of saturation (S_r) and height (h) can be seen in Table 3.

After filling and closing the cell, the bottom RH/T sensor was installed. To insert it the block of bentonite was drilled (Figure 4, left) with a bit of the same diameter as the sensor (12 mm). The material expelled during drilling was recovered and weighed (the corrected initial weight and volume are indicated in Table 3). Afterwards, the sensor was quickly inserted. The pore pressure sensor was fixed to the upper lid of the cell (Figure 4, right). The pressure sensors were screwed to the cell body in contact with the external surface of the bentonite cylinder.

Test CT32	w (%)	h (cm)	ρ_d (g/cm^3)	S_r (%)	Volume (cm^3)	Dry mass (g)
Pellets/Powder mixture	7,2	7,24	1,50	24	1.286,7	1.930,2
Block	8,2	7,24	1,50	27	1.286,7	1.930,2
Average / (Total)	7,8	14,48	1,50	25	2.573,4	3.860,5
After drilling	-	-	-	-	2.562,9	3.853,0

Table 3. Initial characteristics of the materials of test CT32

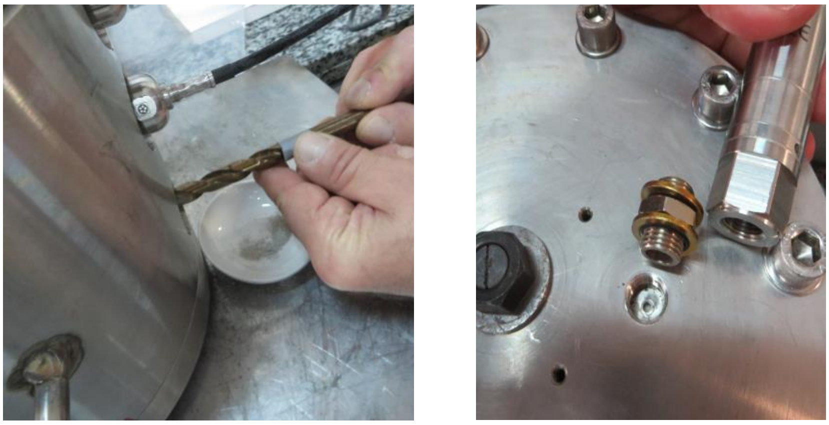

Figure 4. Drilling the hole for the placement of the bottom RH/T sensor (left) and upper pore pressure sensor (right)

The data recorded by the RH/T sensors once installed and before the start of operation are shown in Figure 5. The values measured by the three sensors once inside the bentonite were very similar and were correlated with the slight initial difference in water content of the pellets (7.2 %) versus the block (8.2 %). Hydration started one day after the cell was assembled.

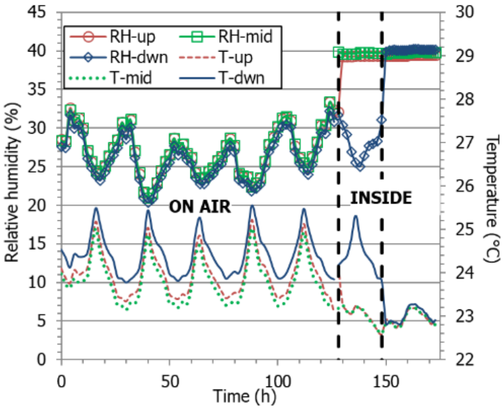

Figure 5. Recordings of the RH/T sensors on air and inside the cell before hydration. The dashed vertical lines indicate the moment different sensors were inserted

The values measured by the sensors just before hydration are shown in Figure 6. They would correspond to an initial suction of 130 MPa. The pore pressure sensor recorded an initial value of 95 kPa.

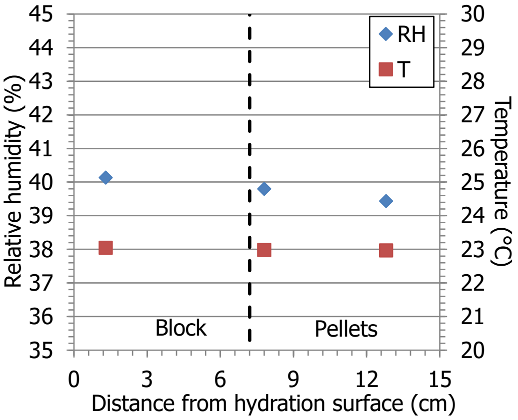

Figure 6.   RH/T inside the cell just before hydration

5 ONLINE RESULTS

Deionised and degassed water was injected at a pressure of 0.014 MPa using a GDS volume/pressure controller. The water intake was faster at the beginning: in the first 1.5 h the water intake was so quick that the injection pressure could not reach the target value. It is considered that most of this water filled the hydration ducts inside the bottom lid and the lower porous stone. This value was in fact checked at the end of the test, when the cell was dismantled (see section 6.2), and has been subtracted from the initial water intake as shown in Figure 7. Considering this correction, and after approximately 650 days, the water intake stabilised at a value of ~861 cm^3, which would correspond to a final water content of 30 %. During this time, gas bubbles were occasionally observed in the hydration line, which had to be periodically vented.

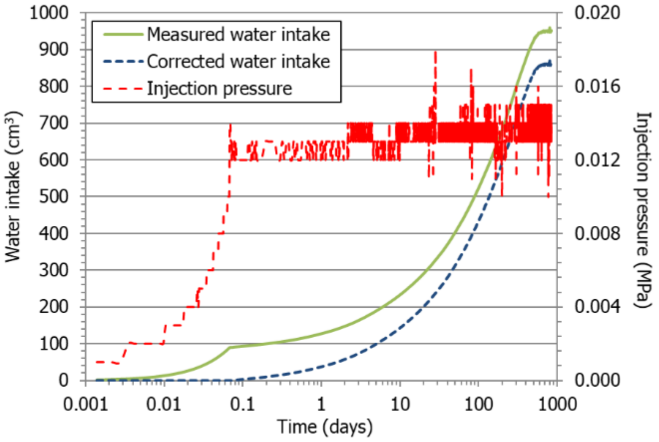

Figure 7. Measured and corrected water intake and injection pressure in test CT32

The RH sensors' recordings during the whole test duration are shown in Figure 8. They evolved at different speeds. The one closest to the water inlet (bottom), located inside the block at 13 mm from the hydration surface, was the first to record an increase from the initial value (in less than 1 h), in accordance with the fast initial water intake, and reached 100 % in about three weeks. The middle and upper sensors (both in the pellet-powder zone) started to record increases according to the proximity to the hydration front, i.e. after 2.5 and 10 days of hydration, respectively. Despite this fast reaction to hydration, it took more than1 year for the sensor in the middle of the cell to record 100 %. The upper sensor failed after 312 days of hydration, when it was recording 93 %. It resumed operation after 645 days of hydration for a short period of time, giving values of 100 %. After 1.5-2 years of hydration, consistently with the stabilisation of water intake, the RH at all positions inside the bentonite was around 100 %. All the sensors stopped providing data before the end of the test, likely because they were flooded. The temperature inside the bentonite during hydration was 22±2 ˚C, reflecting the changes in the laboratory temperature, but with no other evolution pattern.

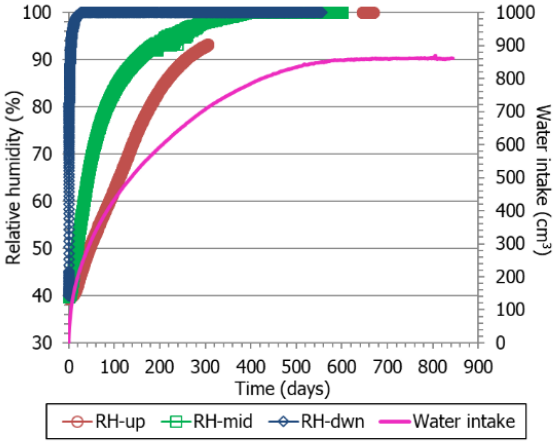

Figure 8. Relative humidity and water intake evolution during hydration (up: 12.8, mid: 7.8, dwn: 1.3 cm from the hydration surface)

The pressure sensors operated correctly since hydration started but with greater oscillation towards the end of the experiment, perhaps due to causes unrelated to the behaviour of the bentonite, such as electronic issues (Figure 9). The bottom sensor recorded a quick and steady pressure increase just after 8 days of hydration. After ~700 days it stabilised in values that kept in 3.7±0.1 MPa until the sensor stopped working a few days before the end of the test. The pressure in the middle of the cell experienced a very soft initial increase between ~10 and 30 days, a subsequent soft decrease, and then increased very steeply to values close to 4 MPa in less than 100 days. Afterwards, it very softly decreased and later increased in the period between 100 and 400 days, when the increase rate rose until reaching an approximately steady value after 650 days that remained until the end of the test in 5.3±0.2 MPa. The upper sensor recorded initially a very sharp decrease that lasted 50 days, simultaneously with the increase in pressure recorded at the bottom of the cell, and subsequently a very sharp increase until a value of ~1 MPa followed by a soft decrease and, after 300 days, started to steadily increase again. After 700 days a steady value of 6.0±0.1 MPa had been reached, the highest measured in the cell.

The pore pressure sensor on top of the cell increased during the first ~360 days and then it decreased sharply until day 562, when it started to increase again very sharply until day ~700. Then it increased more softly until day ~800, when an equilibrium value of 227±1 kPa was reached.

It is remarkable that the stabilisation of the pressure values, which occurred in a narrow period between ~645 and 790 days, took place shortly after no more water was taken by the bentonite (~625 days, Figure 8), but taking more time for the upper radial pressure and the pore pressure.

A summary of the values recorded by the sensors during operation is given in the Appendix.

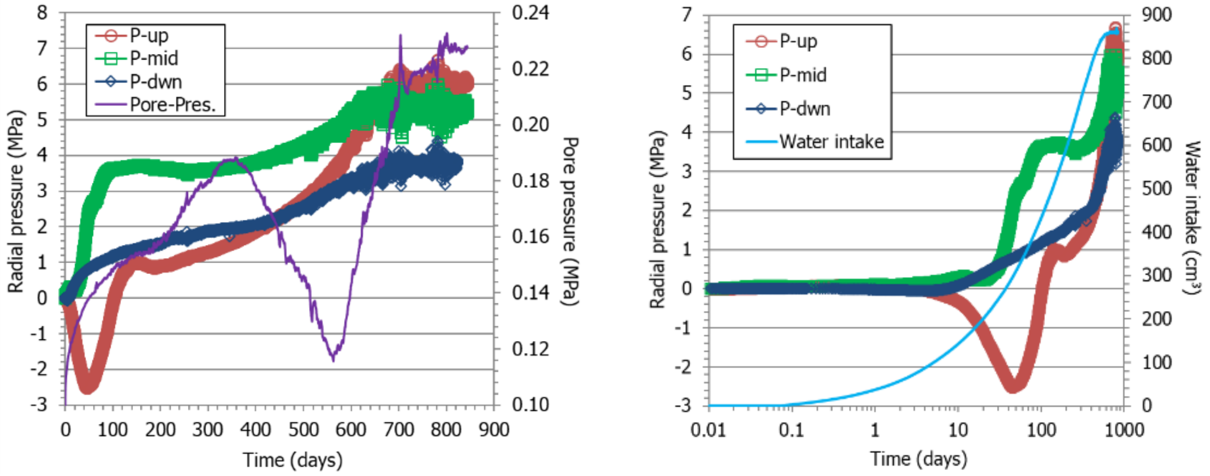

Figure 9. Radial pressure (P-up: 12.8 cm, P-mid: 7.8 cm, P-dwn: 1.3 cm from hydration surface), pore pressure and water intake evolution during the hydration phase in lineal and log scales

6 CELL DISMANTLING AND SAMPLING

The cell dismantling was accomplished on November 11th 2024, after 844 days of hydration, and comprised two phases. The first one, consisting of ending hydration, disconnecting cables and tubes and removing sensors; and the second one consisting of the extraction and sampling of the bentonite column. The whole process was carried out in the same laboratory.

6.1 ENDING OF OPERATION

The first dismantling phase followed the steps described below, with indication of the exact time of some of the operations:

- The data acquisition interval was changed to 1 minute (8:59).
- The water injection line was closed (8:59).
- The pore pressure sensor was removed and the opening closed (9:09).
- The sensing elements of the RH sensors were removed first, because the stainless steel filters were stuck inside the bentonite and had to be removed afterwards (see point 6 below). The upper RH/T sensor (extracted 9:12-9:20) as well as the middle one (extracted 9:20-9:24) had some water inside. The bottom RH/T sensing element had some rust (removed 9:27-9:29).

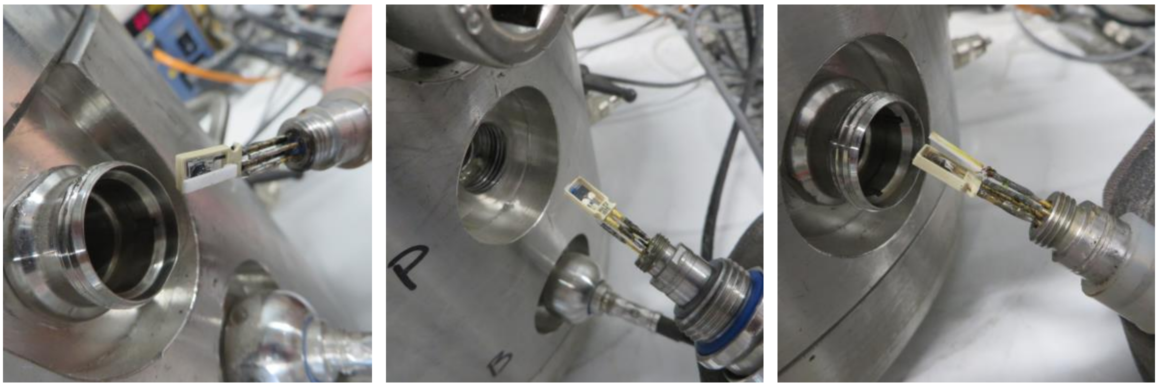

Figure 10. Removal of upper (left), middle (middle) and bottom (right) RH/T sensing elements

- The pressure sensors were disconnected and removed with a pipe wrench. The upper (extracted 9:32), middle (extracted 9:34) and bottom one (extracted 9:36) were found to be clean (Figure 11). As the sensors were removed, the threaded holes in the cell were plugged with nuts to prevent water loss.

Figure 11. Removal of pressure sensors and appearance of these

- The stainless steel filters of the RH/T sensors were removed by screwing them in a bespoke piece that was used to pull them out, but only the upper one was intact. The other filters were broken and remained inside the bentonite (Figure 12). Upon extraction, the voids left were filled with Teflon plugs.

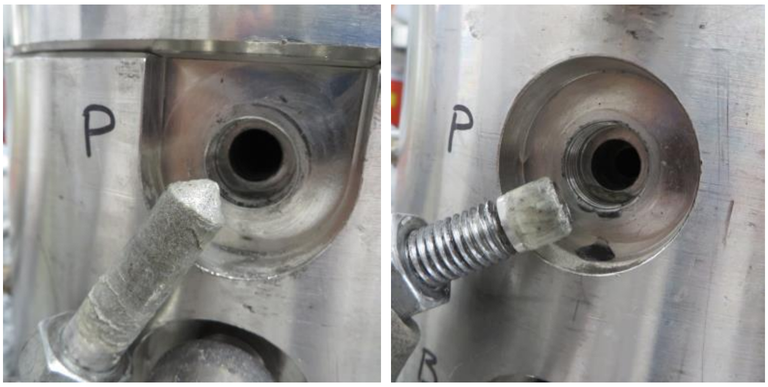

Figure 12. Sinter filters of the upper RH/T sensor (left) and of the middle sensor (right)

- From 9:37 the time of data acquisition was changed to 1 hour and the sensors were left measuring in the air to check their performance.

6.2 CELL DISASSEMBLING AND BLOCK EXTRACTION

The second dismantling phase proceeded following approximately the steps described below.

- The cell was weighed before disassembling it (Figure 13).
- The top cover was removed. The filter paper that had initially been placed on top of the bentonite retained its initial appearance, but was adhered to the bentonite and was difficult to detach from it (Figure 14, left). The exposed area was covered with plastic film during subsequent handling to prevent moisture loss.

Figure 13. Weighing of the cell before disassembling

- The bottom cover was removed. The porous stone through which hydration took place showed numerous black spots, particularly on the external part, and a certain sulphurous odour. The black spots on the porous stone could correspond to areas of fungal growth (Figure 14, middle). The filter paper that had been placed between the bentonite and the porous filter was intimately adhered to the bentonite (Figure 14, right).

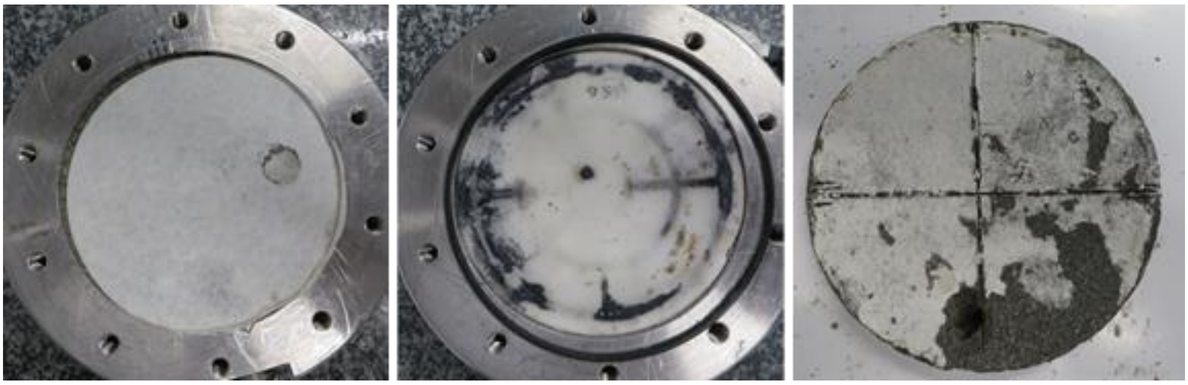

Figure 14. Upper filter paper (left), bottom porous stone (middle) and bottom filter paper (right) upon dismantling

- The clay block was extracted from the cell using a steel piston placed on top of the sample to which pressure was applied with a press (Figure 15). The bentonite came out into a hollow steel cylinder placed below the testing cell. The impact of the sample on the bottom surface was cushioned by a layer of rubber and paper. The sample maintained its cohesiveness and consistency during extraction, handling, section cutting and subsequent sampling.

- The bentonite block was photographed, measured and weighed (Figure 16), as well as all the elements that came out with it (porous stone, filter paper, sinter filters and Teflon plugs) and the clay adhered to the inside of the cell and auxiliary elements. The block was then protected with plastic film, to avoid loss of mass during subsequent manipulations and cuttings.

Figure 15. Extraction of the sample from the cell using a uniaxial press, steel piston on top and auxiliary cylinder below

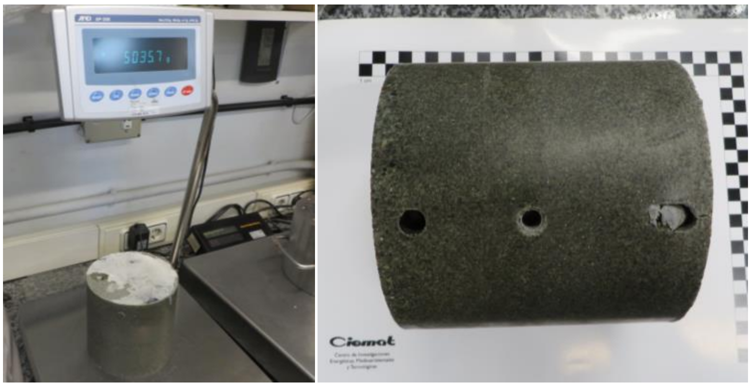

Figure 16. Final weighing of the block and appearance (hydration surface on the right hand side)

The bentonite block had a homogeneous appearance, it was dark and no pellets or other distinctive elements could be told apart. In fact, the separation between pellets and block was not clear, but it seemed to be at ~7.2 cm from the bottom surface (Figure 17, left). Upon extraction, the final height of the sample was 14.53 cm, slightly higher than the initial one (14.48 cm, Table 3) No change in diameter was detected. Hence, the dry density of the block once extracted would be 1.50 g/cm^3.

The elements of the cell (porous stone, filter papers, top and bottom lids, sensors' filters) were weighed just after disassembling and then again once they were clean and dry, which allowed to compute the water taken by the cell elements, approximately 60 g. Most of it was probably taken at the very beginning of the experiment (the bottom porous stone took ~56 g of water), and for this reason this quantity has been subtracted from the initial water intake, as shown in Figure 7.

The final weight of the bentonite was calculated considering all the intermediate weights taken for the different elements during the process described above. The most realistic value obtained was 5017 g, which implies that the bentonite took 868 g of water, in good agreement with the online measurement. According to the theoretical initial and dry weights of the sample (Table 3), this would correspond to a water content of 30.2 % and a degree of saturation of 99 %.

6.3 BENTONITE SAMPLING AND ASSESSMENT OF FINAL STATE

The bentonite sample was consistent and easy to handle and it could be easily sectioned using a saw. Saw cuts were made to obtain seven slices or horizontal/transversal sections (Figure 17, Figure 18), covering the compacted block area (sections 5B-7B), the pellets area (sections 1P-3P), and the contact area between both (section 4BP). In order to obtain an overall (approximate) value of the density of each section, they were weighed (Figure 17, right) and measured with a calliper.

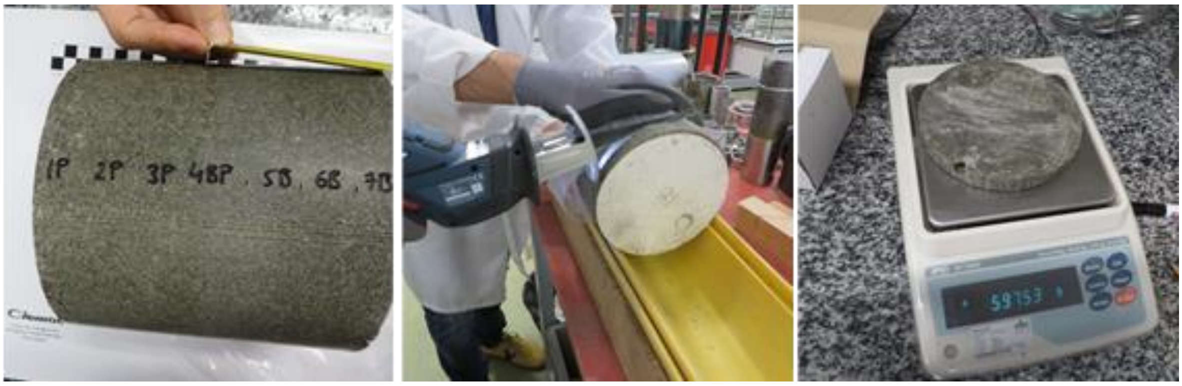

Figure 17. Definition of slices (left), cutting of a section (middle) and weighing of the slice obtained (right)

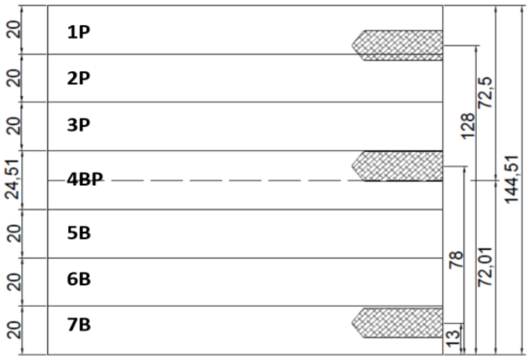

Figure 18. Schematic representation of the subsampling of the bentonite block in horizontal slices (1P to 7B) and indication of the position of the RH/T sensors on the right (dimensions in millimetres, values according to initial measurements)

Within each section a series of samples were taken to analyse the state of the bentonite in the inner, outer and intermediate areas of the bentonite column. For this purpose, a cross-shaped scheme covering the three areas was followed. Figure 19 gives an example of the subsampling done in section 1P, and the same information is given in the Appendix for the other sections. For each slice, four samples were obtained in the external ring, four in the middle ring and a central sample, i.e. a total of nine samples per slice. Each of these samples was cut into two pieces, one was used for water content and dry density determination (samples ρ) and the other one for water content measurement (samples w). The remaining four quadrants were numbered 1 to 4 and parts of them were used for other types of analyses (MIP, BET, XRD and gas conductivity along the pellets/block interface).

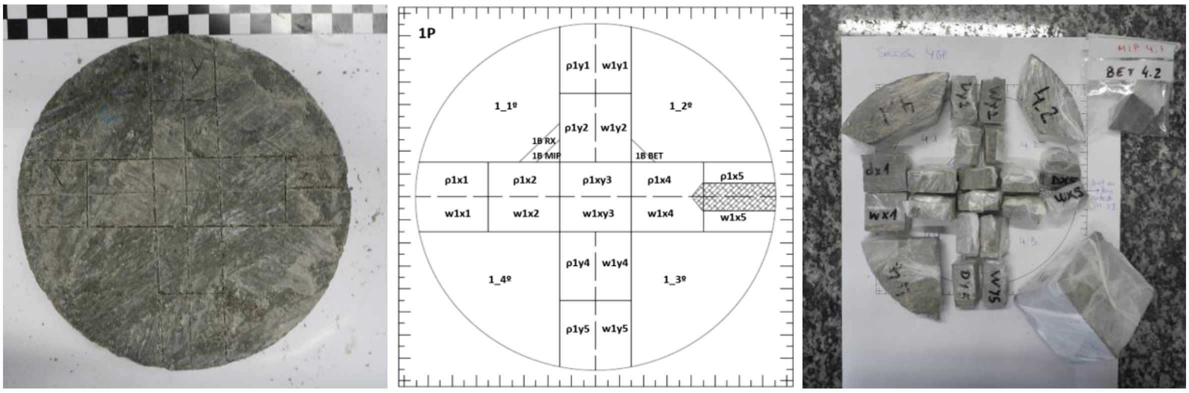

Figure 19. Appearance of a section before being cut into subsamples (left), sampling scheme with reference to the type of determination (ρ: dry density, w: water content, RX: XRD, MIP, BET), and subsamples obtained (right)

The samples from section 4BP, containing the block/pellets contact, were more carefully inspected. It was not easy to tell apart mixture from block (Figure 17, left).

7 ASSESSMENT OF SENSORS PERFORMANCE

Once the RH/T sensors and filters were removed from the bentonite they were left reading uncleaned inside capsules with silica gel for about two weeks, since none of the sensors was providing RH measurements. This procedure brought all the sensors to measure very similar values between 40 and 45 % (Figure 20, left). Afterwards they measured in air for about 5 days until they were cleaned. Once cleaned, they continued to record values for a month (Figure 20, right). At all stages, they recorded very similar values among them. Figure 21 shows the measurements of pressure and pore pressure sensors after dismantling. The measurements in air of these sensors were similar to those recorded before the start of the test, except for the P-dwn sensor, which had stopped working before the end of the test due to electronic causes. The changes in the pore pressure measurements are due to atmospheric pressure variations.

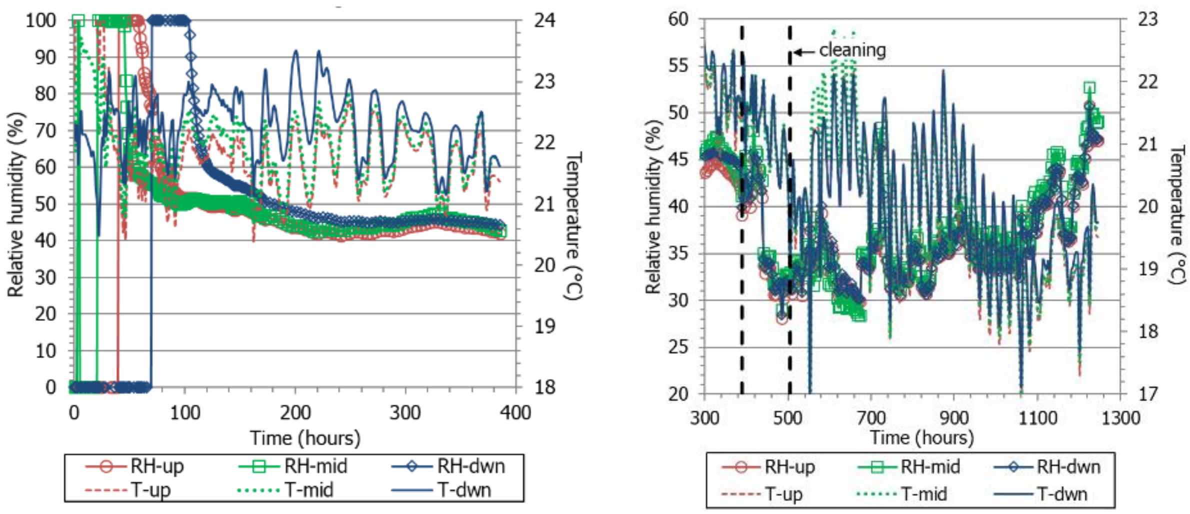

Figure 20. Recordings of RH/T sensors after extraction: inside silica gel (left), in air before and after cleaning (right)

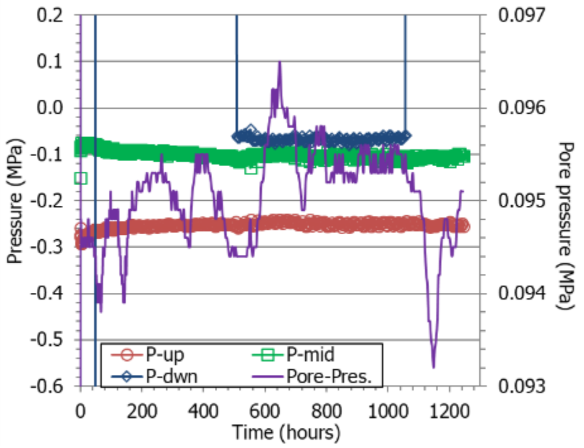

Figure 21. Recordings of the pressure sensors in air after dismantling

8 FINAL STATE OF THE BENTONITE

8.1 DRY DENSITY AND WATER CONTENT

8.1.1 METHODOLOGY

The gravimetric water content (*w*) is defined as the ratio between the mass of water and the mass of dry solid expressed as a percentage. The mass of water was determined as the difference between the mass of the sample and its mass after oven drying at 110 °C for 48 hours (mass of dry solid). The samples used for the water content determination had masses between 7.7 and 19.8 g, with an average of 11.3±2.3 g.

Dry density (ρ_d) is defined as the ratio between the mass of the dry sample and the volume occupied by it prior to drying. The volume of the specimens was determined by immersing them in a recipient containing mercury and by assessing the weight of the mercury displaced, considering a density of mercury of 13.6 g/cm^3. The absolute error of this measurement is in the order of 10^{-2} g/cm^3. The volume of the samples used for this determination ranged between 4.6 and 13.0 cm^3, with an average of 7.5±1.4 cm^3. The same samples whose volumes had been determined were used for an additional water content determination (subsamples ρ in Figure 19). However, this value was only used as a cross-check and the water content determined in dedicated samples (just oven dried, subsamples w in Figure 19) was the one used to compute the dry density.

The balance used was an AND GF2000, with a capacity up to 2,100 g and a precision of 0.01 g.

8.1.2 RESULTS

The values obtained are summarised in Table 4 to Table 6, where average values for slice and area (external, middle and internal) are included. The values obtained for each sample are shown in the Appendix. The average water content of the bentonite column would be 29.3 %, which is slightly lower than the value reported in 6.2 obtained from the final weight (30.2 %). This is reasonable, since even careful handling of wet samples cannot avoid certain drying during manipulation. The final dry density obtained from the final column dimensions (1.50 g/cm^3) is slightly lower than the average obtained from the different measurements (1.51 g/cm^3). The resulting degree of saturation is 97 %.

Slice	Distance to hydration (cm)	*w* (%)	*w* ext (%)	*w* mid (%)	*w* int (%)	*w* isolines (%)
1P	13.45	27.8	28.2	27.3	27.7	27.8
2P	11.45	27.0	26.7	27.4	27.4	-
3P	9.45	27.7	27.5	28.1	28.1	-
4BP	7.23	29.5	29.4	29.6	29.6	29.5
5B	5.00	30.2	30.2	30.3	30.5	-
6B	3.00	30.4	30.4	30.4	30.1	-
7B	1.00	33.2	33.5	32.8	31.9	33.0
Average	-	29.3	29.4	29.4	29.3	-

Table 4. Water content measured in subsamples according to their position (ext: average of 4 measurements at 6.1 cm from the axis, mid: average of 4 measurements at 3.4 cm from the axis, int: measurement at the axis)

Slice	Distance to hydration (cm)	ρ_d (g/cm^3)	ρ_d ext (g/cm^3)	ρ_d mid (g/cm^3)	ρ_d int (g/cm^3)	ρ_d isolines (g/cm^3)
1P	13.45	1.55	1.54	1.56	1.55	1.55
2P	11.45	1.56	1.57	1.54	1.57	-
3P	9.45	1.55	1.55	1.54	1.54	-
4BP	7.23	1.51	1.51	1.51	1.51	1.51
5B	5.00	1.49	1.49	1.48	1.49	-
6B	3.00	1.48	1.48	1.49	1.49	-
7B	1.00	1.42	1.41	1.43	1.45	1.42
Average	-	1.51	1.51	1.51	1.51	-

Table 5. Dry density measured in subsamples according to their position (ext: average of 4 measurements at 6.1 cm from the axis, mid: average of 4 measurements at 3.4 cm from the axis, int: measurement at the axis)

Figure 22 shows the water content and dry density values obtained along the bentonite column and Figure 23 the degree of saturation computed from them. The water content was higher in the 3 cm closest to the hydration surface, increasing towards it, but decreased from the middle of the block towards the upper surface. As it was to be expected in samples fully saturated, the dry density followed a pattern inverse to that of water content. The water content determined in the external ring of the block, i.e. in the bentonite in contact with the cell wall, was higher than the internal one both at the bottom and on top of the block. Conversely, the dry density on these areas was consistently lower. This could mean that, at least initially, the cell wall was a preferential path for water, especially along the vertical line of the RH/T sensors (see Figures in Appendix). Away from the bentonite column ends, the water content and dry density distributions at a given horizontal level were more homogeneous. The degree of saturation ranged for most samples between 96 and 98 % and, unexpectedly, was lower close to the hydration surface.

Slice	Distance to hydration (cm)	S_r (%)	S_r ext (%)	S_r mid (%)	S_r int (%)	S_r isolines (%)
1P	13.45	98	98	98	98	98
2P	11.45	97	97	96	100	-
3P	9.45	97	97	98	98	-
4BP	7.23	98	98	98	98	98
5B	5.00	97	97	96	98	-
6B	3.00	96	96	97	96	-
7B	1.00	96	96	97	96	96
Average	-	97	97	97	98	-

Table 6. Degree of saturation measured in subsamples according to their position (ext: average of 4 measurements at 6.1 cm from the axis, mid: average of 4 measurements at 3.4 cm from the axis, int: measurement at the axis)

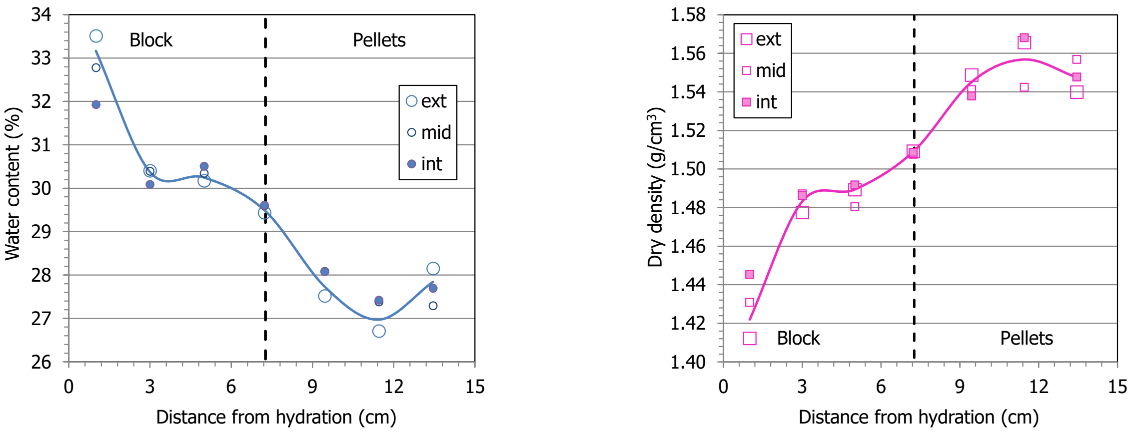

Figure 22. Water content and dry density measured across the sample (ext: average of 4 measurements at 6.1 cm from the axis, mid: average of 4 measurements at 3.4 cm from the axis, int: measurement at the axis)

Isolines have been interpolated between these values, and 2D graphs of different sections across the column have been obtained with Surfer (Golden Software Inc.) (see Appendix). The water content and dry density distribution of a vertical section across diameter X (parallel to the diameter where the RH/T sensors were placed) can be seen in Figure 24. The Figure highlights the higher water content at the bottom and at the external ring of the top and the inverse correlation with dry density. The software used to draw these graphs allows computation of mean values of the different parameters. Some of them are also included in the Tables above, and perfectly agree with those obtained by weighted average of all the measurements for a given area.

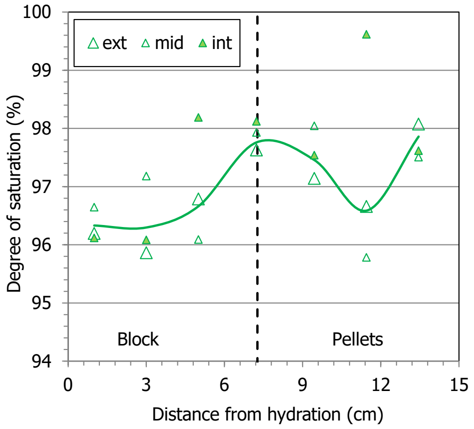

Figure 23. Degree of saturation measured across the sample (ext: average of 4 measurements at 6.1 cm from the axis, mid: average of 4 measurements at 3.4 cm from the axis, int: measurement at the axis)

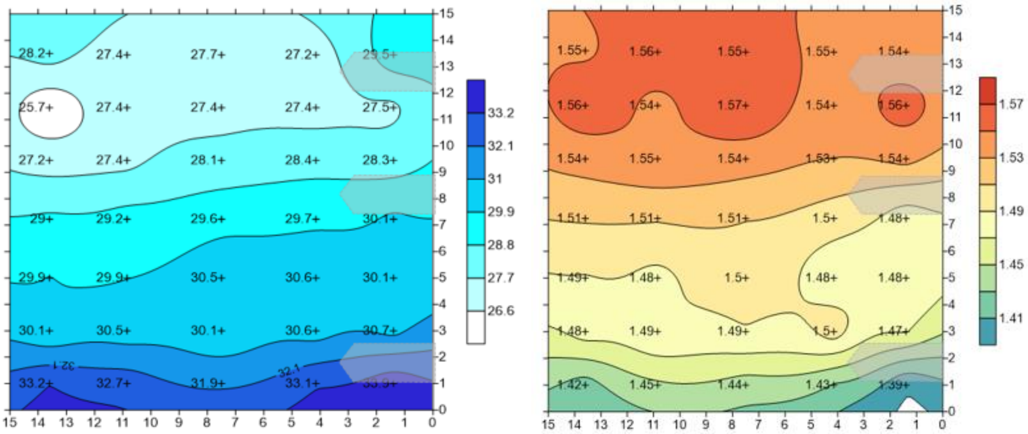

Figure 24. 2D contour representations of water content (%, left) and dry density (g/cm^3, right) of the vertical section along the X diameter (see Figure 19 for location). The position of the RH/T sensors is indicated with shadowed forms

8.2 PORE SIZE DISTRIBUTION AND SPECIFIC SURFACE AREA

8.2.1 *METHODOLOGY*

The pore size distribution of some of the subsamples from the intermediate ring of each section was determined by mercury intrusion porosimetry (MIP). This technique allows the determination of the pore size distribution by injecting mercury into the sample at different pressures while measuring the volume intruded. The pressure applied may be related to the minimum pore diameter intruded taking into account the characteristics of the fluid (Washburn equation). The ratio of the volume of mercury intruded (pore volume) to the applied pressure (which conditions the minimum pore diameter) allows distribution curves to be obtained establishing the percentage of pores of a size included within a given interval.

The pores of the sample have to be empty, i.e. free of water, before the mercury intrusion test. In order to minimise the alteration of the clay microstructure during water removal, the samples were immersed in liquid nitrogen to avoid the formation of large ice crystals, given the instantaneous freezing achieved at the liquid nitrogen temperature of -196 °C. Afterwards, they were put in the ice condenser of a Telstar LioQuest equipment at -30 °C for 3 hours. Subsequently, they were lyophilised for 22 hours at a temperature of -50 °C under a vacuum of 0.2 mbar, so that to eliminate the water in the pores by sublimation. Thereafter, they were heated at 25-30 °C for 3 hours. The samples were later kept in a desiccator until the MIP analysis. The mass of the subsamples was between 0.9 and 1.1 g. The porosimeter was a Micromeritics AutoPore Series IV 9500, which allowed the exploration of pore diameters between 0.007 and 600 µm. Prior to mercury injection the sample was outgassed by applying a vacuum of 50 µm-Hg. Afterwards the mercury injection pressure was increased from 2.7 kPa to 220 MPa in 109 steps. To determine the extrusion branch of the curve, pressure was released in 56 steps down to a pressure of 68.6 kPa. A contact angle of mercury of 139° both on advancing and of receding on the clay surface was considered.

The mercury intrusion method allows access to be gained only to part of the macroporosity (pores of diameter smaller than ~550 µm) and to part of the mesopores (those of sizes between 50 and 7 nm), since mercury does not intrude the microporosity (pores of a size of less than 2 nm, according to the classification of Sing et al. 1985). Actually, the percentage of pores intruded by mercury in the samples analysed in this work was between 65 and 81 % (see next section). In the compacted and saturated bentonite from test CT32, pores larger than those that can be quantified by MIP are not expected. Hence, considering that most of the non-intruded porosity corresponds to the pores of a size smaller than the limit of the apparatus (7 nm), an estimation of the percentage of pores actually intruded can be made by comparing the actual void ratio of the samples (computed from their dry density and density of solid particles) and the apparent void ratio calculated from mercury intrusion. Thus, the pore size distribution curves obtained by MIP were corrected to take into account the percentage of pores not intruded. There is uncertainty in this approach, since it is possible that pores larger than 7 nm were not intruded because of the bottleneck effect: the pores connected to the external surface by narrow openings will not be intruded until sufficient pressure is applied to intrude the entryways. All of the volume of such pores will be allocated to the threshold radius class of the most restricted part of the entryway, which will result in an overestimation of the smaller pore sizes volume.

The nitrogen sorption isotherms were determined in an ASAP 2020 of Micromeritics. The samples were lyophilised (as for the MIP samples explained above) and ground in an automatic agate mortar for 3 minutes. Aliquots of between 1.3 and 1.8 g were degassed at 90 °C for the time necessary to reach a vacuum of 50 µm Hg, which was kept for 10 min. Afterwards the samples were kept at 90 °C under vacuum for 500 minutes. The isotherms obtained had 60 points, 36 in the range of relative pressures between 0.01 and 0.99 (adsorption) and 24 points in the range between 0.99 and 0.14 (desorption). The BET method (Brunauer et al. 1938) was applied in the range of P/P_0 0.06-0.2 to compute the external specific surface area, i.e. the surface of the intra-aggregate and inter-aggregate voids but not that of the interlayer space. This value is a measure of the degree of coherent stacking of smectite platelets (Sposito 1992).

8.2.2 RESULTS

Figure 25 shows the incremental curves of mercury intrusion as a function of the mean pore diameter of the diameter size intervals corresponding to each pressure increase step for MX-80 samples of the same characteristics (reference curves) as the initial conditions used in the cell (block and pellets/powder mixture, see Table 3 for a reminder of the initial conditions of both materials). For the block part, the curve corresponding to a sample compacted at dry density 1.5 g/cm^3 with a water content of 9 % was used as representative of the initial state. For the GBM, a mixture of pellets/powder with a ratio 70/30 was prepared in the sample holder and slightly pressed. Although the density reached was much lower than the actual dry density of the mixture in the test (0.75 *vs.* 1.5 g/cm^3) the curve obtained probably displays the main features of the pore size distribution of the mixture. The Figure also shows the pore size distribution corresponding to single pellets with no powder addition. Obviously, the porosity of the high-density pellets was much lower, with practically pores of size larger than 100 nm. The distribution for pore sizes below ~10 µm was similar for the pellets and for the mixture, but for larger pores there was a huge difference, since the individual pellets do not have large pores. The curve obtained for the mixture showed a predominant pore size around 150 µm (likely smaller for the actual mixture initial dry density). Both in the mixture and in the compacted block, two major pore families could be identified, the separation between them being set at ~200 nm, approximately separating macro and mesopores.

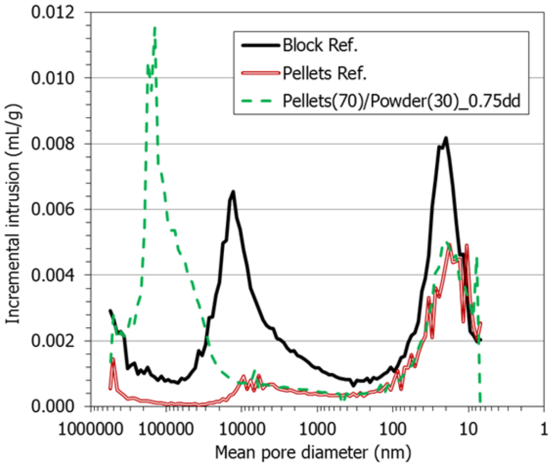

Figure 25. Pore size distribution expressed as incremental mercury intrusion of initial materials used in test CT32

Figure 26 shows the incremental curves of mercury intrusion for the subsamples of test CT32. The figure also includes the curves corresponding to the reference initial materials discussed in the previous paragraph. As a result of hydration, the macroporosity of the block samples decreased and shifted to larger pore sizes. Additionally, a new macropore family emerged towards sizes that were smaller (from 1000 to 100 nm) as the sample was closer to the hydration surface. The volume corresponding to pores smaller than 200 nm decreased but the mode kept in the same values. The volume of macropores in the mixture (those that can be explored by MIP) decreased in all samples and the pore size modes shifted to lower sizes. In the mixture samples the volume of mesopores increased, but their mode size remained the same.

The percentage of void ratio intruded, the void ratio corresponding to each pore size interval and the respective modes are shown in Table 7. The void ratio corresponding to each pore family for the different samples is shown in Figure 27 as a function of the distance to the hydration surface. As well, the mean sizes of the two pore families are shown on the right-hand side of the Figure. At the end of the test, the microstructure of the two parts, mixture and block, had evolved towards more similar pore size distributions, because of the significant decrease in macroporosity and the increase in mesoporosity of the mixture. The same occurred in the block part, but to a smaller extent. Although the initial values for the pellets/powder mixture are uncertain, it is clear that both in the mixture and in the block, hydration entailed an increase in the void ratio corresponding to pores smaller than 200 nm and a decrease in the void ratio of the larger ones, particularly for the mixture. The sample closest to the hydration surface, 7B, behaved differently to the others (the void ratio corresponding to both mesopores and macropores increased slightly), likely owing to the more significant density decrease (to 1.44

g/cm^3) (Figure 22). The mean pore sizes that can be explored by MIP did not change significantly, except for a clear decrease for the macropore size in the mixture and an increase of it in the sample closest to the hydration surface.

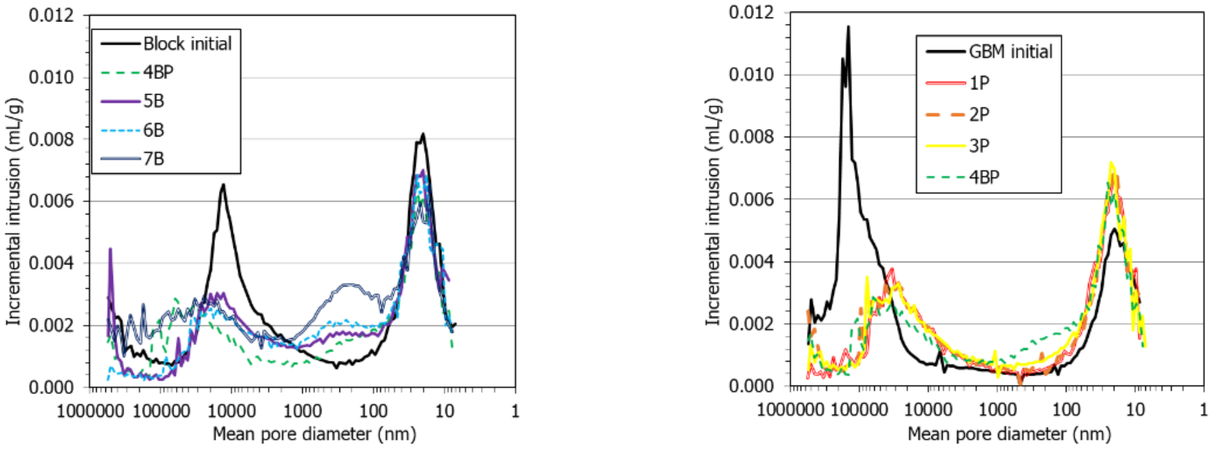

Figure 26. Incremental mercury intrusion in subsamples from test CT32 and of the initial materials (see Figure 18 for the location of samples)

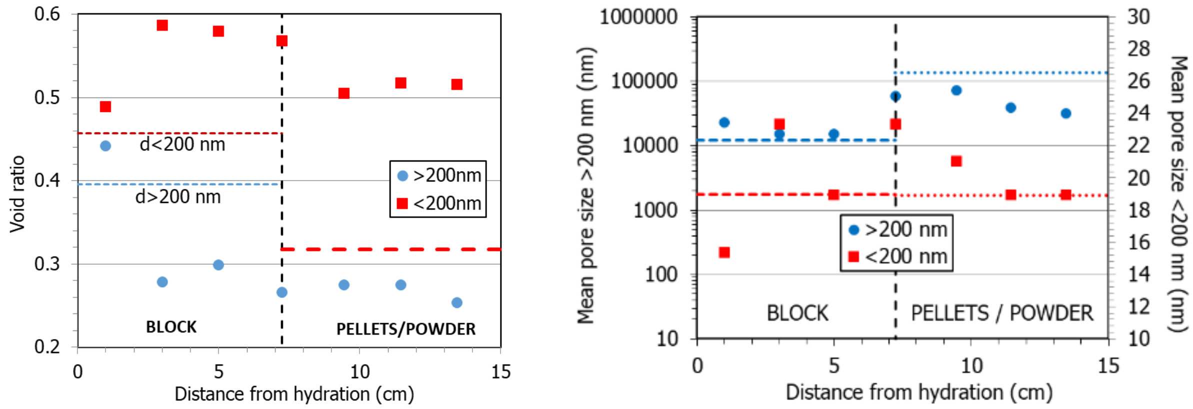

Figure 27. Void ratio corresponding to different pore sizes (left) and mean pore size (right) obtained by MIP in samples from test CT32 (the thick horizontal lines indicate the values for the reference block and GBM; the initial macropore void ratio for the GBM was probably higher than 2, not shown in the Figure)

The BET specific surface area of the samples was between 26 and 32 m^2/g (Table 7), lower for the block samples, which is probably a consequence of the different initial specific surface area of pellets and powder (31 *vs*. 25 m^2/g). There was no particular relation between the location of the samples or their water content and the specific surface area.

Ref.	Distance to hydration (cm)	Intruded *e* (% of total)	*e* pores >200 nm (-)	Mode pores >200 (nm)	*e* pores <200 nm (-)	Mode pores <200 (nm)	**BET a_s (m^2/g)**	*t*-plot μ-pore volume (cm^3/g)	d_{001} (nm)
1P	13.45	67	0.253	31,721	0.515	18.9	31	0.004	1.473
2P	11.45	68	0.275	39,143	0.517	18.9	27	0.004	1.517
3P	9.45	70	0.275	73,317	0.505	21.0	32	0.004	1.529
4BP	7.23	65	0.266	59,504	0.568	23.4	24	0.002	1.549
5B	5.00	68	0.299	15,236	0.579	18.9	31	0.004	1.473
6B	3.00	67	0.279	15,233	0.587	23.4	26	0.002	1.514
7B	1.00	81	0.442	23,204	0.489	15.4	30	0.004	1.578
Block	-	83	0.396	12,362	0.457	19.0	-	-	-
Pellets	-	88	0.072	5,517	0.238	17.1	31	0.004	-
Powder	-	24	-	205,617	-	19.0	25	0.004	~1.25
GBM	-	24	2.375	135,332	0.318	18.9	29a	0.004[a]	-

[a] computation from the pellets and powder values considering a 70/30 ratio

Table 7. Pore size distribution obtained with MIP, BET specific surface area from nitrogen adsorption isotherms and basal spacing of samples from test CT32 (e: void ratio)

8.3 BASAL SPACING

8.3.1 METHODOLOGY

The (001) reflection or basal spacing gives the distance along the crystallographic *c*-axis between clay lamellae, and for a given clay depends on the exchangeable cations present in the interlayer and their degree of hydration.

After dismantling, subsamples from each slice were preserved in paraffined foil and the X-ray profile of a plane surface of them was registered at laboratory temperature after removing the foil and without any further treatment. The samples were X-rayed within 24 h after dismantling.

An anticathode of Cu (CuKα) radiation was used with a Philips model X'Pert-MPD diffractometer (Bragg Brentano configuration) at 40 mA, 45 kV operating condition. X-ray diffraction (XRD) experimental profiles were obtained with a fixed divergence slit size 0.6 mm, receiving slit size 5 mm and a scanning rate of 0.025 °2θ/s. Data were collected between 3 and 10 °2θ. The complete mathematical description of the scan pattern was obtained by combination of a polynomial function that describes the background and a profile function that fits the experimental peaks in order to obtain better peak parameters (peak position, net intensity and full width at half maximum (FWHM)). The pseudo-Voigt profile function, which is the weighted mean between a Lorentz and a Gaussian function, was used to fit the reflections as well as to deconvolute overlapped peaks.

8.3.2 RESULTS

The basal reflection was measured by XRD: Fragments of the samples were X-rayed trying to keep the final water content unchanged by avoiding any accidental drying. The XRD patterns showed a double (001)-reflection that could be decomposed into two diffraction peaks by profile fitting (Figure 28). The main peak was in a range between 1.58 and 1.47 nm, corresponding to the full development of the 2-layer hydrate. The secondary one corresponded to the transition to the 3-layer hydrate (values between 1.64 and 1.81 nm), except in sample 1P, for which the secondary peak corresponded to a lower spacing than the main one. In most cases the two peaks were very close and difficult to tell apart, only the sample closest to the hydration surface (sample 7B) had a distinct secondary peak which additionally corresponded to the 3-layer hydrate (Figure 28, right). The values of the main diffraction peak of the basal reflection are shown in Table 7. In both parts, mixture and block, they were higher towards the hydration surface. The top and bottom of the column showed the lowest and highest values, respectively, which may be related to the difference in water content.

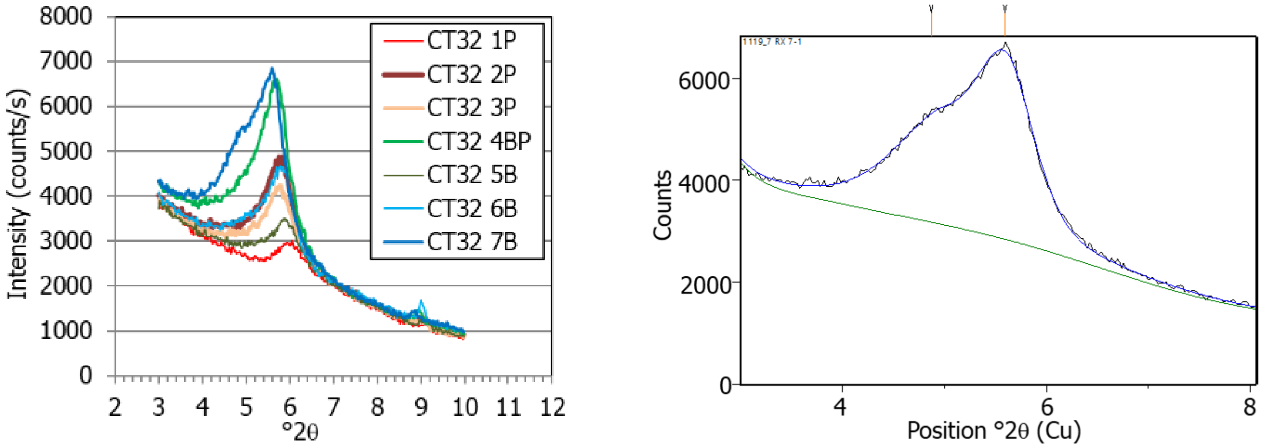

Figure 28. XRD patterns of untreated samples (left) and detail for sample 7B (right)

9 HEALING OF MIXTURE/BLOCK INTERFACE: GAS TESTING

At the end of the test, a cylindrical subsample was obtained by drilling across the GBM/block interface (sample 4BP) to measure the gas breakthrough pressure as an indicator of the healing of the interface, as had already been done in related tests using FEBEX bentonite (Gutiérrez-Rodrigo et al. 2021, Villar et al. 2021b). This subsample was vertically crossed by the interface (Figure 29).

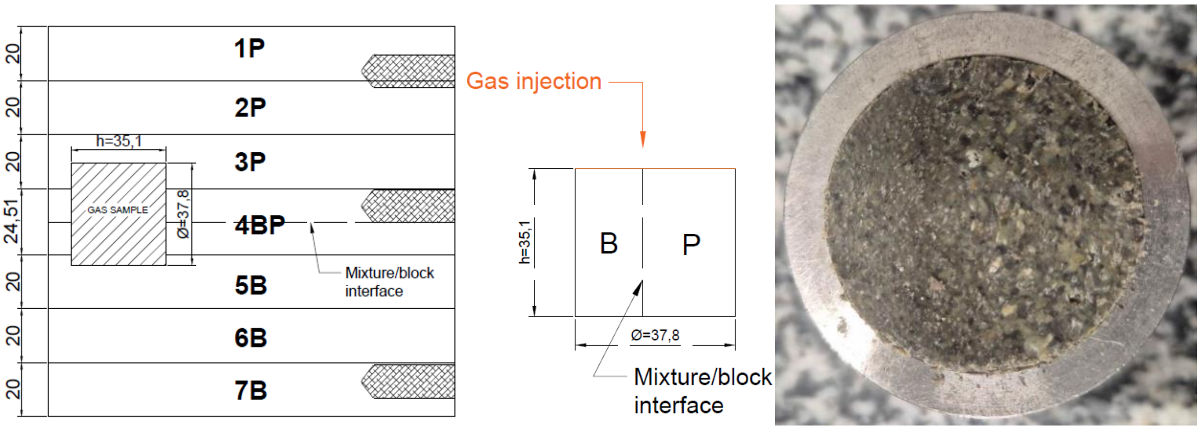

Figure 29. Location of the core trimmed for gas testing and its appearance once inside the testing cell

The core diameter was fit to 3.8 cm by using a cutting ring and knife. Filter paper and porous stones were placed on top and bottom of the sample and it was laterally wrapped in double latex membranes. Vacuum grease was applied between membranes in order to prevent the loss of gas. The wrapped sample was placed in a triaxial cell which was filled with deaired water and pressurised to ensure perfect adherence of the membranes to the surface of the sample and avoid gas transport along it. The cell inlet, at the upper part of the sample, was connected to a nitrogen gas cylinder applying the gas injection. The outlet of the cell, connected to the bottom of the sample, was open to atmosphere, with a series of different range gas mass flowmeters measuring the gas outflow. More experimental details about the equipment and the equations used to compute permeability are given in Villar et al. (2018, 2021b).

The initial and final characteristics of the sample as well as those of the gas test are shown in Table 8.

An initial confining pressure of 4 MPa was applied, corresponding approximately to the swelling pressure of the bentonite with a dry density of 1.51 g/cm^3 (the value for sample 4BP,

Table 5) according to Equation 1. This value was selected to keep approximately the same stress state as the bentonite likely had at the end of the hydration test, when full saturation had been reached, and prevent the interface from mechanically splitting. Prior to gas injection this confining pressure was kept for 33 days. Afterwards, the injection pressure was increased in 0.1-MPa increments every 48 hours, from 0.4 to 3.5 MPa. Since no outflow was recorded, the confining pressure was increased to 5.5 MPa and the injection pressure was increased from 3.5 to 5.3 MPa again in 0.1 MPa increments. The membrane was pierced in the upper part at some moment between 4.2 and 4.4 MPa, allowing for the entrance of some water from the triaxial cell inside the sample. Since no distinct gas flow had occurred so far, the test was dismantled. The pressure and flow evolution during the gas testing are shown in Figure 30. It can be considered that the breakthrough pressure of this sample was higher than 4.2 MPa.

Variable	**Initial**	**Final**
ρ_d (g/cm^3)	1.53	1.52
h (cm)	3.51	3.53
ϕ (cm)	3.78	3.77
w (%)	28.7	28.2
S_r (%)	97	96
Confining P (MPa)	4.0-5.5	-
Injection P (MPa)	0.4-5.3	-
Duration (days)	182	-

Table 8. Initial and final characteristics of the sample used for gas testing (CT32-4BP) and characteristics of the test

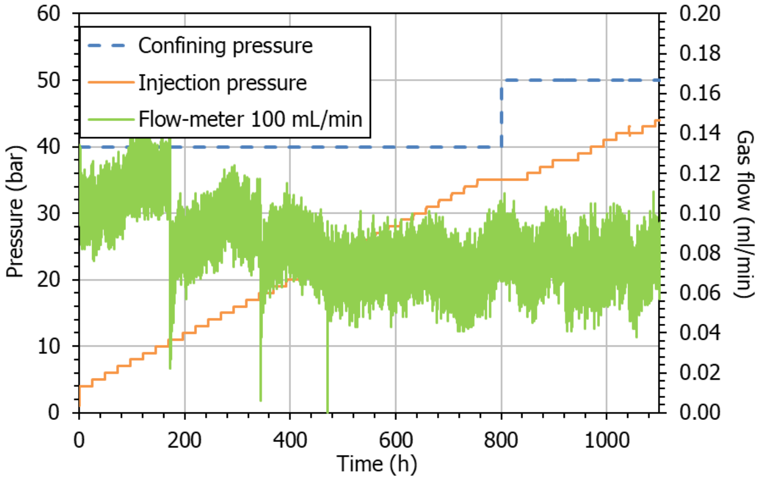

Figure 30. Confining pressure, injection pressure and outflow in gas injection test for sample 4BP of test CT32

Upon dismantling the sample was measured, weighed, and cut into three horizontal sections (top, middle and bottom part of the specimen) where the dry density and water content were determined following the methodology described in subsection 8.1.1. It was checked that the water content was higher in the upper part of the sample, around the area where the membrane was pierced, and there was a water content gradient from top to bottom (from 29.1 to 27.1 %), with a value at the bottom lower than the initial one, which could indicate that some gas was able to cross the sample, even if the volume was too low to be measured by the flowmeters. Hence, and despite the accidental wetting of the top of the sample, the final water content was slightly lower than the initial one (Table 8).

Figure 31 shows the pore size distribution of a subsample taken from the bentonite core after the gas permeability test along with the pore size distribution of a sample taken at the same distance from the hydration surface as that of the sample used for gas testing (i.e. sample 4BP in Figure 26). In all cases the subsamples used for MIP testing included the interface. The consolidation occurred during gas testing reduced the size and volume of the largest macropores (the mode size decreased from 59 µm to values between 39 to 54 µm), as well as that of those in the range 1000-50 nm, which disappeared. As well, the void ratio corresponding to macropores decreased with respect to sample 4BP, except in the top sample. In fact, the sample on top, through which gas was injected, showed some “peaks” in the incremental intrusion corresponding to the largest pores that could indicate the creation of fissures. This, along with the accidental wetting, could have caused the overall macropore volume increase of this sample. As for the volume of pores smaller than 200 nm, it overall decreased with respect to that of sample 4BP.

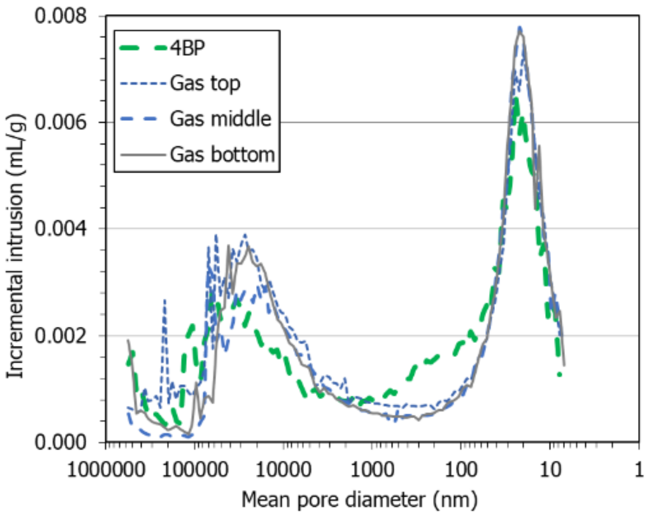

Figure 31. Pore size distribution obtained by MIP of samples of test CT32 before and after gas testing

10 DISCUSSION AND COMPARISON WITH TEST CT31

The test presented, along with the twin test CT31 (Villar et al. 2024), allowed to follow the hydro-mechanical evolution of a two-component (block and pellets/powder mixture, GBM) buffer material upon hydration under isochoric conditions at ambient temperature. The initial dry density of the two components was the same and the water contents were similar. Both parts were manufactured from Wyoming-type bentonite. Hydration took place through the bottom, i.e. through the mixture part in test CT31 and through the block part in test CT32. During the tests, the water intake, the relative humidity and radial pressure at three different levels, and the pore pressure on top were measured.

10.1 HYDRO-MECHANICAL EVOLUTION

Even though the water injection pressure was very low (0.014 MPa), the initial water intake was quick in the two cells, due to the high bentonite suction (120-130 MPa). It was quicker in the test saturated through the mixture (CT31), because of its large macroporosity (Figure 25) and higher initial permeability, where the powder filling the voids between pellets was a low-density preferential pathway. It has to be taken into account that at the beginning of the tests, 44 % of the GBM volume corresponded to powder (see section 4). The final water intake stabilised in similar values for both cells after ~600 days (Figure 32), corresponding to final water contents of 31 and 30 % and degrees of saturation of 100 and 99 % for cells CT31 and CT32, respectively. These are approximate values, given the uncertainty about the water that remained in the bottom porous stone and sensor filters.

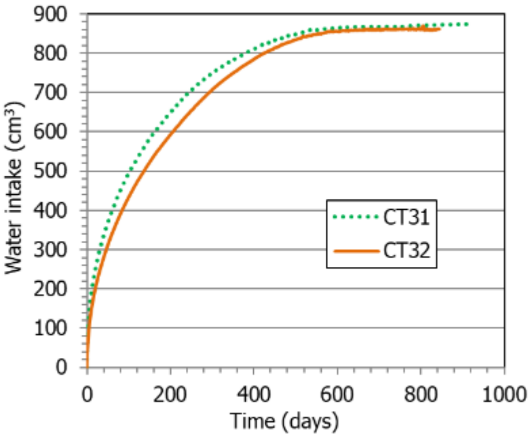

Figure 32. Water inflow in both cells under an injection pressure of 0.014 MPa

The RH evolution followed a similar pattern in both tests: it started to increase earlier as the location was closer to the hydration surface and eventually reached 100 % (Figure 33). In the bottom and middle sensors the RH increase started earlier in cell CT31, in accordance with the faster initial water intake in this cell. Also, the bottom sensor in cell CT31 measured 100 % earlier than in cell CT32 (1 *vs.* 27 days). However, the middle and upper RH sensors recorded values of 100 % earlier in test CT32 than in CT31 (Figure 33, right), even though, according to the water intake, the time for full saturation was similar in both tests. This would indicate that water redistribution inside the bentonite continued to take place after overall full saturation had been reached, and that this took more time in the block (placed on top in cell CT31) than in the mixture.

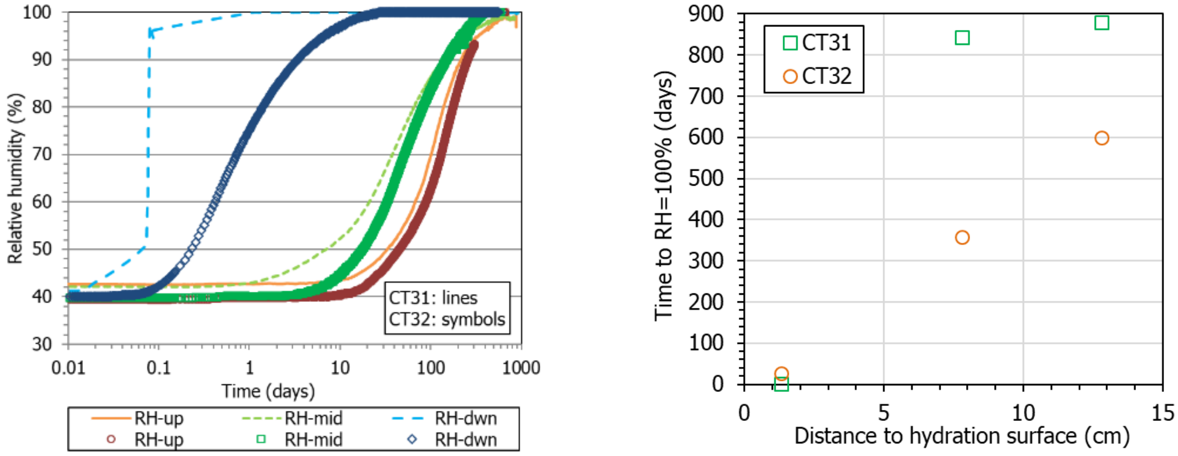

Figure 33. Relative humidity evolution at three distances from the hydration surface (up: 12.8, mid: 7.8, dwn: 1.3 cm) in the two tests (left) and time elapsed before the RH sensors recorded 100 % at each location (right)

The radial pressure started to increase first at the location of the bottom sensor, then at the middle one and finally at the top one (Figure 34). At the bottom of the cells, radial pressure increased very quickly and steadily, with an intermediate period of softer decrease in both cells and higher values always in cell CT31, perhaps in agreement with the higher relative humidity in the area (Figure 33). The equilibrium pressure value was reached earlier and was higher in test CT31 than CT32. In the middle of the cell the pressure development pattern was very similar in the two tests, with a sharp initial increase followed by a soft and prolonged decrease that ended up in a relevant increase up to the steady values, which were reached shortly after 600 days in the two cells. The major difference in radial pressure development was found in the sensors placed farthest from the hydration surface, because of the significant initial decrease in cell CT32, absent in cell CT31. However, after the first year, the radial pressure at this location in the two cells evolved similarly, reaching steady values around 6 MPa after approximately 700 days. The initial decrease recorded on top of cell CT32 took place as soon as pressure started to increase at the bottom sensor location (after 10 days), which would indicate a significant collapse of the mixture placed in the upper half of the cell, prompted by its high macroporosity.

The collapse observed later in the middle part of both cells was much less significant, but more relevant in cell CT32.

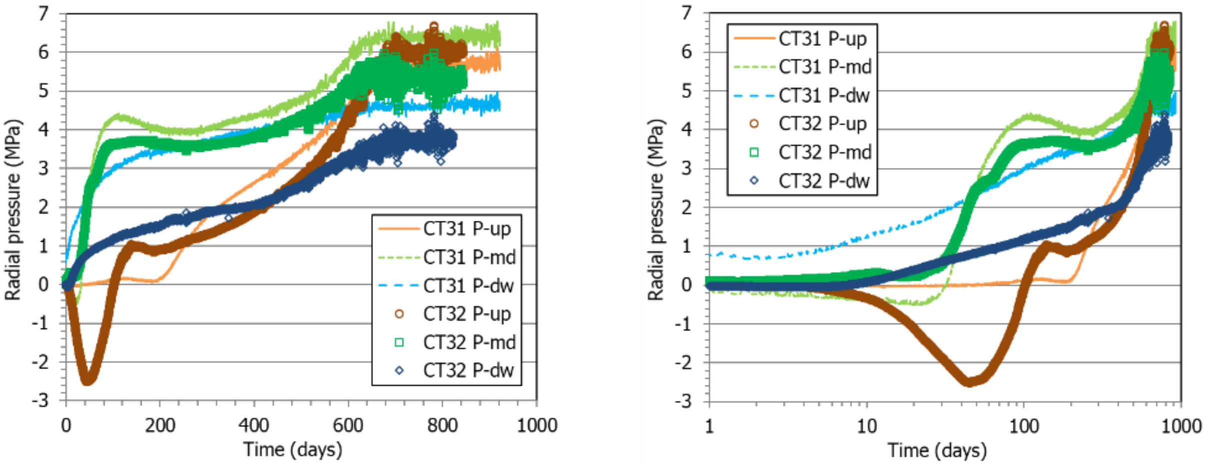

Figure 34. Evolution of radial pressures at three distances from the hydration surface (up: 12.8, mid: 7.8, dwn: 1.3 cm) in the two tests in linear and log scale

The pore pressure on top also evolved differently in the two cells: for more than 500 days it did not change in the case of cell CT31, whereas in this period it significantly increased and then sharply decreased in cell CT32. When the overall degree of saturation of the bentonite (according to the water intake) was higher than 98 %, the pore pressure started to increase at a high rate in both cells, until reaching a stable value, that was higher in the case of cell CT32, after more than 700 days (Figure 35).

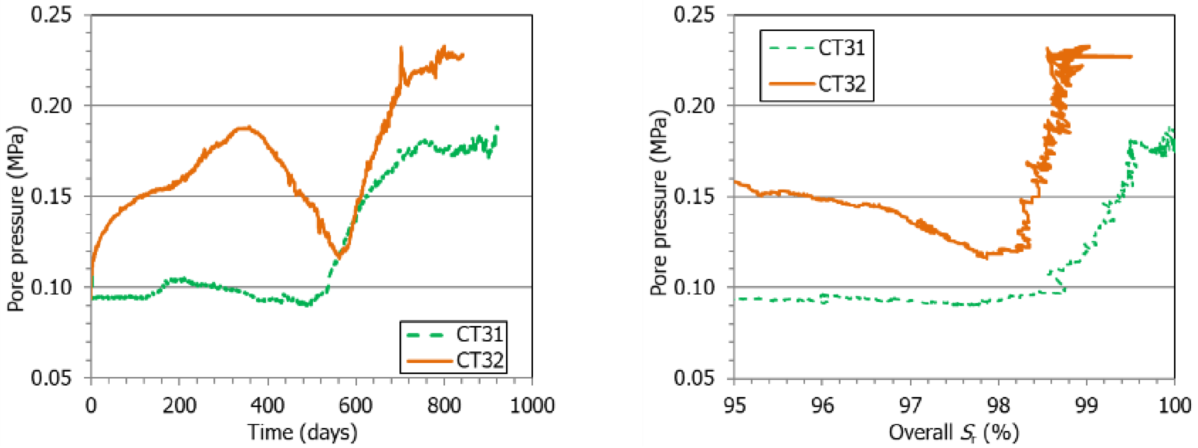

Figure 35. Evolution of pore pressure on top of the cell in the two tests as a function of time (left) and of the overall degree of saturation of the bentonite at the final stage of the tests (right)

As the previous figures show, the pressure values stabilised in all cases after 600 days, whereas the water intake had already stabilised around this time (Figure 32). Figure 36 enlarges the time period over which pressures stabilised for both cells, with an indication of the approximate moment when it happened for each sensor (as dashed vertical lines). These times are plotted as a function of the location of the sensors in Figure 37. The differences between the pressure stabilisation times for both cells were significant only at the bottom and on top (pore pressure). The Figure also shows the radial pressure equilibrium values at each location, which were higher for cell CT31, except at the top of the sample. This could be related to the slightly higher final water content of cell CT31 and longer duration.

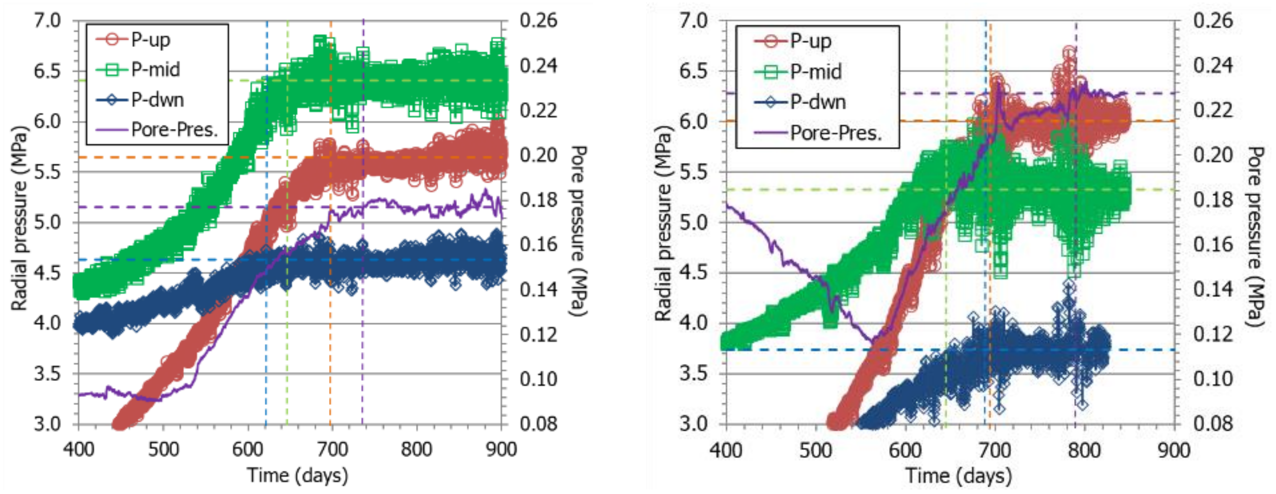

Figure 36. Final evolution of radial and pore pressure in tests CT31 (left) and CT32 (right)

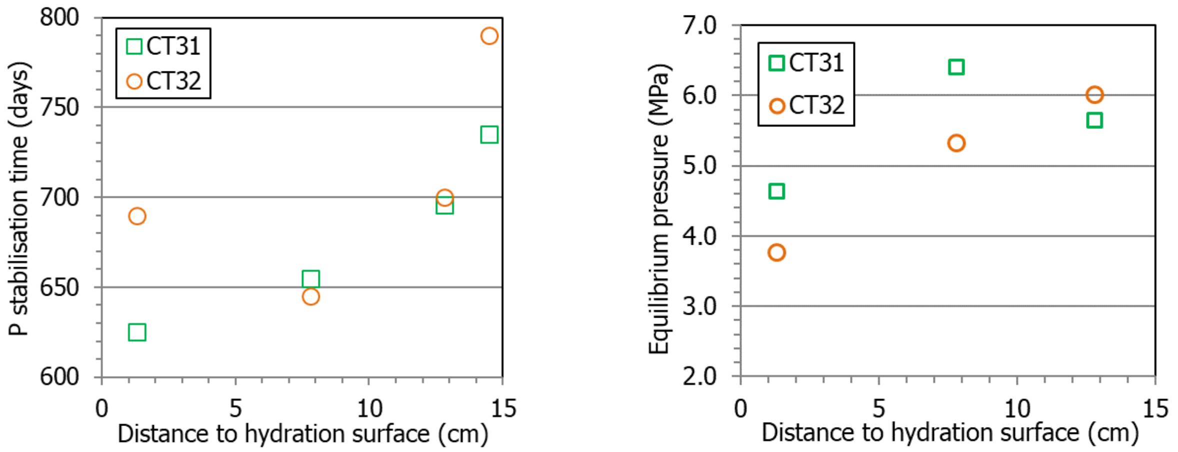

Figure 37. Time for stabilisation of radial and pore pressure for the two tests (the values for 14.5 cm correspond to pore pressure) and equilibrium radial pressure (right)

The relation between the relative humidity and stress changes at a given location (Figure 38) shows that the sensors closest to the hydration surface became quickly flooded, and in both cases no pressure increase was recorded in the area until RH was higher than 95 %, despite the fact that they were placed in different materials (GBM mixture in test CT31 and compacted block in CT32). As well, at the location of the top radial pressure sensors (12.8 cm from the hydration surface), most pressure build-up occurred when RH was higher than 90 %. In the middle part of the cells, although significant radial pressures (~up to 4 MPa) developed progressively for RH<90 %, major increases were also recorded when the RH in the area was close to 100 %. Hence, at all locations, significant pressure increases occurred for small RH increments close to saturation. In the EB in situ test performed at the Mont Terri URL, where a large-scale two-component barrier (FEBEX GBM and blocks) was tested for 10.5 years, most of the sensors installed in the bentonite recorded relative humidity values of 100 % only one year after the beginning of the test, whereas it took four years for the total pressure sensors to record stable values that kept approximately constant until the end of the test (García-Siñeriz et al. 2015). This was interpreted by Villar et al. (2021a) as a demonstration that the mechanism that triggered most of swelling was the redistribution of water in the microstructure. In the case of sodic bentonites, such as MX-80, it is known that osmotic swelling, which is particularly relevant when the degree of saturation is very high, may be the largest component of swelling, overcoming the crystalline one.

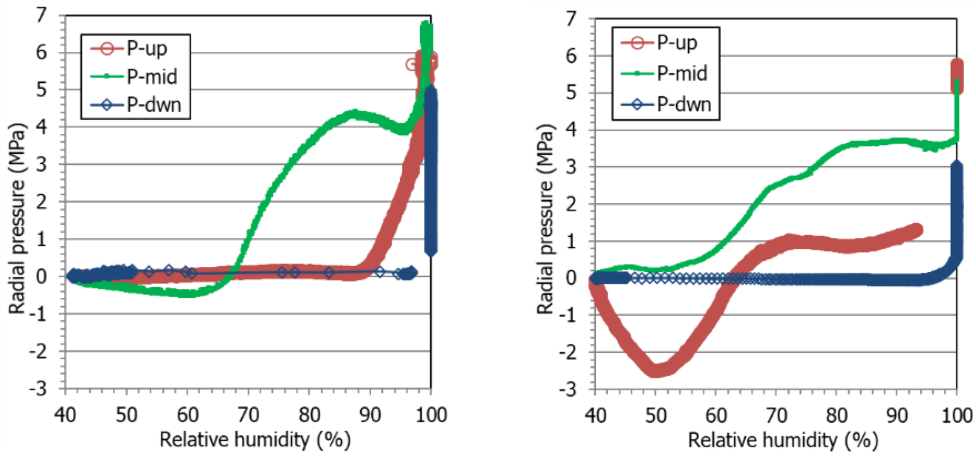

Figure 38. Radial pressure measured at different heights against the relative humidity in the same locations in test CT31 (left) and CT32 (right). See Figure 2 for location of sensors

10.2 FINAL PHYSICAL STATE

The cells were dismantled when no further water intake was recorded and relative humidity and pressure had been stable for long, although test CT31 run for longer (922 *vs*. 844 days). Upon dismantling of the cells, the bentonite column (composed of the two parts, block and GBM) was extracted, measured and weighed. The bentonite had a similar appearance in both cases (dark, wet) and a consistent state, with no pellets identifiable and with a separation between the block and the GBM very subtle, difficult to tell apart (Figure 39). The 3D reconstruction of images taken by micro-computed tomography of sample 4BP (block/GBM interface) of test CT31 clearly showed the interface between both parts as an area with lower porosity (Villar et al. 2024). These 3D reconstructions also highlighted the different porosity of the two components and areas of different porosity inside them. Postmortem gas testing along the block/GBM interface in cell CT32 showed that not only sealing, but also complete healing of the interface had been reached, since no gas flow took place along this interface even for gas pressures as high as 5.3 MPa (see subsection 9).

Figure 39. Appearance of the material extracted in test CT31 (left, GBM in the lower half) and CT32 (right, compacted block in the lower half). Hydration from the bottom

The difference between the final and initial bentonite weight gives an indication of the actual water intake during the tests that allows to compute overall water contents, which were 30.5 and 30.2 %, for cells CT31 and CT32, respectively. The extracted columns were subsampled and water content by oven drying and dry density were determined. Most of the bentonite subsamples had water contents between approximately 27 and 34 % and dry densities in the range between 1.42 and 1.56 g/cm^3 (Figure 40). The average water content of the bentonite according to these measurements would be 30.0 and 29.3 % for cells CT31 and CT32, respectively, in accordance with the slightly higher water content of cell CT31 determined by difference between the final and initial total bentonite weight inside the cells. As it was commented in section 8.1.2, the manipulation of subsamples to determine their water content by oven drying may cause some drying that explains the difference. These values agree also with those obtained from the online water intake measurement commented above, and would confirm the slightly higher final water content of cell CT31.

In the upper part of the cells, there was a significant difference between both tests: in test CT32 (mixture on top) the dry density was higher and the water content lower than in test CT31 (block on top). It is remarkable that both the water content and the dry density around the mixture/block interface (middle part of the column) were similar in the two tests. In fact, the mixture/block interface did not seem to have had any effect on the continuous gradients observed, i.e. there were no sudden changes across the interface. This had already been observed for a related series of tests of similar configuration, using a block and a pellets mixture of FEBEX bentonite (Villar et al. 2021a). As well, in the 3 cm closest to the hydration surface the water content and dry density gradients were similar in the two tests: water content was maximum at the hydration surface and decreased upwards, and dry density followed the inverse pattern. This area (the 3 cm closest to the hydration surface) presented significantly higher water contents and lower dry densities than the rest of the bentonite columns, even though the initial dry density of the block and the GBM parts were similar and hydro-mechanical equilibrium seemed to have been reached in both tests. This would indicate that the source of final heterogeneity was not the initial state, but the hydration process itself. In the series of tests reported in Villar et al. (2021) no complete homogeneity in terms of dry density or water content was reached in any case, even for situations very close to full saturation: the water content decreased from the hydration surface to the opposite end whereas the dry density increased, although these gradients tended to attenuate over time and may have dissipated if the tests had lasted even longer (confirmed by unpublished results of test MGR28). These heterogeneities resulted from the initial swelling and ensuing density decrease of the bentonite that became first saturated (those parts closest to the bottom hydration surface), and the consequent compression of the bentonite located upwards. Bernachy-Barbe et al. (2020) found analogous water content and dry density distributions after 600 days of hydration and complete hydro-mechanical stabilisation in a test performed with an MX-80 bentonite mixture of pellets and powder (80:20) of average dry density 1.52 g/cm^3 in a cell of height 10.5 cm (test 240_3).

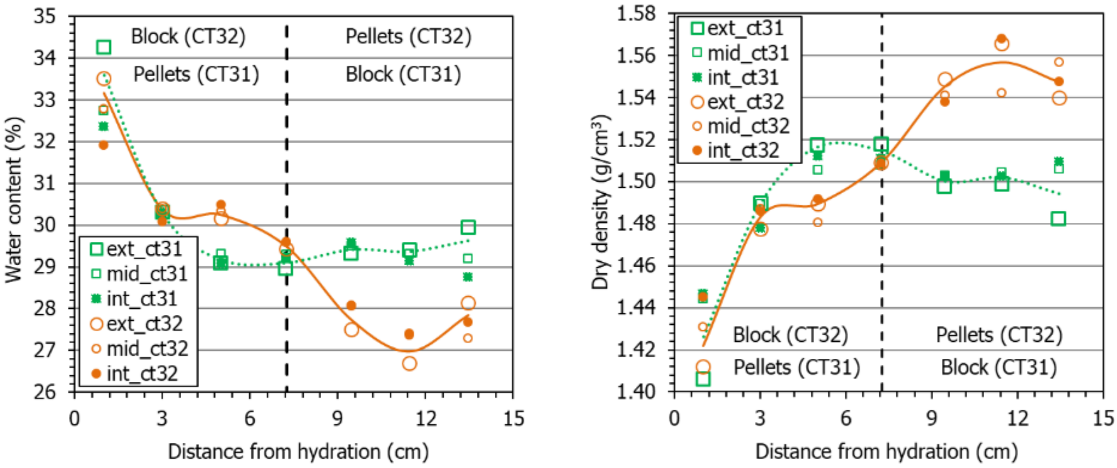

Figure 40. Water content (left) and dry density (right) as a function of distance to hydration surface and position inside the sampling slice (ext: average of 4 measurements at 6.1 cm from the axis, mid: average of 4 measurements at 3.4 cm from the axis, int: measurement at the axis) for the two tests

Despite the fact that no further water intake or pressure changes were recorded in the tests, which suggests that hydro-mechanical equilibrium had been reached, the final measured degrees of saturation were lower than 100 %, in most samples between 95 and 98 % (Figure 41). However, according to the final weight of the columns, the bentonite in the cells had reached degrees of saturation of 100 and 99 % for cells CT31 and CT32, respectively (in agreement with the slightly higher final water content of cell CT31). Hence, the subsamples could have experienced expansion upon extraction from the cell and later trimming, as well as some drying during manipulation, which would explain the degrees of saturation <100 % computed for the subsamples. The higher degrees of saturation and water contents of test CT31 could result from the longer duration of this test. The samples from the mixture half had in the two cells higher degrees of saturation than those from the block part. It is remarkable that, despite the higher homogeneity in water content of cell CT31, its degree of saturation gradient was steeper than for cell CT32.

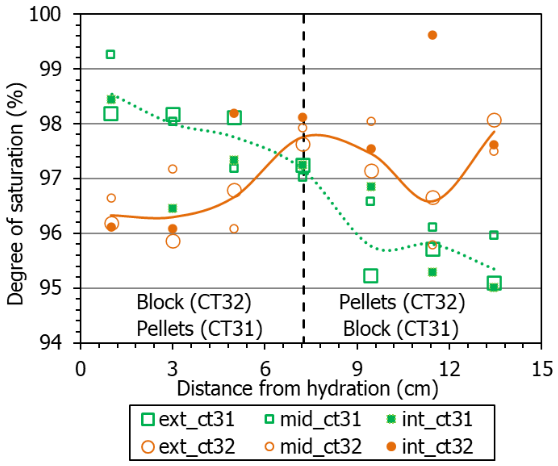

Figure 41. Degree of saturation as a function of distance to hydration and position (external, middle or internal inside each section) of the post-mortem determinations for the two tests

10.3 ANALYSIS OF PRESSURE MEASUREMENTS

Thanks to the detailed determination of dry densities at different locations of the bentonite columns, the final equilibrium pressures measured at three different levels (Figure 37, right) could be related to the dry densities measured at the end of the tests in the area where the sensor was located (Figure 42). Hydration tests performed in large-scale cells where axial and radial pressures were measured at different heights along the sample length showed that during saturation, the transient pressure values were related to the local dry density (Dueck et al. 2016, Bian et al. 2019, Bernachy-Barbe et al. 2020, 2022, Harrington et al. 2020). In fact, the radial pressures measured in cells CT are clearly related to the dry density, increasing with it, and they were clearly higher in test CT31. The empirical exponential correlation between dry density and axial swelling pressure, obtained from tests in standard oedometers (with sample diameters 3-5 cm and heights 1-2.5 cm) in which MX-80 samples compacted to different dry densities were saturated with deionised water (Equation 1), is also plotted in the Figure. From this Equation the axial swelling pressure corresponding to an MX-80 bentonite compacted to the overall dry density of the CT samples (1.5 g/cm^3) would be 3.5 MPa. As well, an evaluation of the relationship between dry density and swelling pressure for the WH2 bentonite (from which the pellets used in this research were manufactured) reported by Bosgiraud and Foin (2016) showed that with a dry density of 1.50 g/cm^3 the swelling pressure obtained at saturation of material would be around 4 MPa. These values are considerably lower than those actually measured in the cells, but they correspond to axial pressures, whereas in the cell only radial pressures were measured.

The experimental results reported in the literature about the relation between radial and axial pressure developed by bentonite on saturation are not entirely consistent. This relation seems to depend on the way the sample was compacted, its density, degree of saturation and particular sample composition (pure bentonite or sand/bentonite mixtures). Dieudonné et al. (2024) consider that there are at least two factors that may contribute to non-homogeneous swelling of bentonite samples: the sample compaction procedure, which is generally uniaxial, hence anisotropic (as it is the case of the block in the CT tests reported here), and the hydration procedure. In a hydration test performed with a bentonite pellets/powder mixture, the axial swelling pressure measured was mostly lower than the radial pressures, although the authors hypothesised that the reason could be a lower average dry density at placement at the upper surface where the axial pressure was measured (Bernachy-Barbe et al. 2020). Åkesson et al. (2009) reported also higher radial than axial pressure during the saturation under thermal gradient of compacted MX-80 bentonite and Rawat et al. (2019) during the isothermal saturation of a bentonite/sand mixture. Other authors working with compacted bentonite or sand/bentonite mixtures found that radial pressures were lower than axial pressures (Lee et al. 2012), but some of them found that the difference between both decreased as full saturation was approached and for high-density samples and high pressures (Pintado et al. 2013, Saba et al. 2014).

An additional reason for the higher than expected pressures measured could be the scale effect, since previous laboratory work showed that the swelling pressure tends to be higher as the testing cell is larger (Imbert and Villar 2006). However, Dieudonné et al. (2024) found a good consistency between the radial stresses measured in a decimetric-scale test performed with a sand/bentonite mixture isotropically compacted and the dry density-swelling pressure trend determined on small-scale samples.

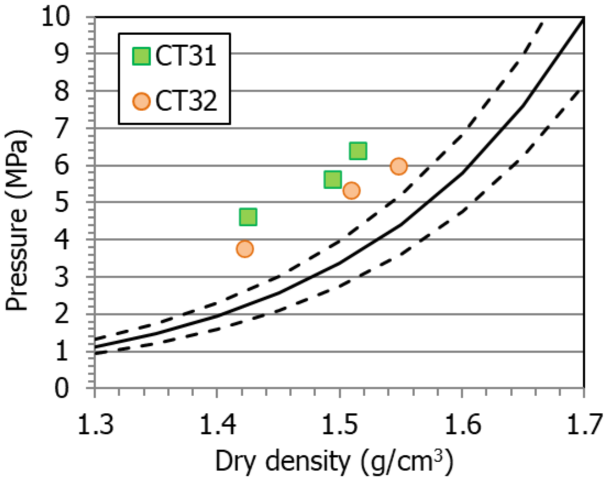

Figure 42. Axial swelling pressure of MX-80 compacted to different dry densities (curves, Eq. 1) and equilibrium radial pressures measured in tests CT31 and CT32 as a function of the final dry density measured at the sensors' locations (symbols)

The tests performed by Martikainen et al. 2018 (reported in Talandier, 2019) were very similar in design and dimensions to the tests presented here (except that the block and the pellet mixture had very different initial dry densities, 1.81 *vs*. 0.90 g/cm^3), with hydration under an injection pressure of 10 kPa taking place through the pellets, which were placed on top. In those tests MX-80 bentonite was also used and the radial pressure developed by the block and the pellets parts were measured in addition to the axial one. Pressures were lower in the axial direction than in the radial one. The axial and radial pressure development in the areas farther away from hydration (i.e. around the block part) displayed the initial peak followed by a decrease and a smooth eventual increase. In tests CT31 and CT32 the radial pressure development also showed intermediate stages of decrease or stabilisation in the middle and upper part of the cells, i.e. further away from the hydration surface, irrespective of the fabric of the material (block or mixture). However, at the bottom of the cells, close to the hydration surface, pressure increased in a steady way, with no intermediate stages of decrease or stabilisation (although in test CT32 there was a period of lower pressure increase rate). This is the area of lower final bentonite density and consequent lower final radial pressure, which suggests that the reason for the absence of an increase-decrease-increase pressure development pattern was the low bentonite density and quick saturation and not the fabric, which would also be the case for the tests in Martikainen et al. (2018). Given the huge initial density differences in those tests, pressures were significantly lower in the pellets than in the block part. The modelling groups involved in a benchmark where these tests were analysed, concluded that this difference was indeed due to the initial contrast of density between the top and bottom of the sample, but also to the friction between the bentonite and the steel cell wall (Talandier 2019). However, the numerical model used by Dieudonnée et al. (2024) was able to reproduce the evolution of radial stress upon saturation of a sand/bentonite mixture isotropically compacted without considering possible friction between the sample and the cell wall. In tests CT31 and CT32 radial pressures were mostly related to the final dry density in the area around the sensor, irrespective of the initial fabric of the material, block or mixture.

10.4 MICROSTRUCTURAL ANALYSIS

Concerning the microstructural modifications during hydration, the external specific surface area (determined by the BET method) of the subsamples of the two tests was mostly between 30 and 36 m^2/g (except for two samples), well above the reference values of the two materials, GBM mixture and powder. This increase was to be expected, since water content is one of the variables that affect the specific surface area as determined by nitrogen adsorption, and water content increased considerably in all the samples with respect to the initial value. This increase could indicate an overall disaggregation of clay particles and decrease of their average size, which would result in an increase of the surface available for nitrogen adsorption. However, the differences among samples were not related to the initial fabric of the sample (GBM or block), distance to hydration surface, or to their water content. The values for test CT31 were systematically higher than those for CT32, even for the same water content, and no clear explanation has been found for this fact, although it could be related to the longer duration of test CT31, that would have allowed for further microstructural evolution.

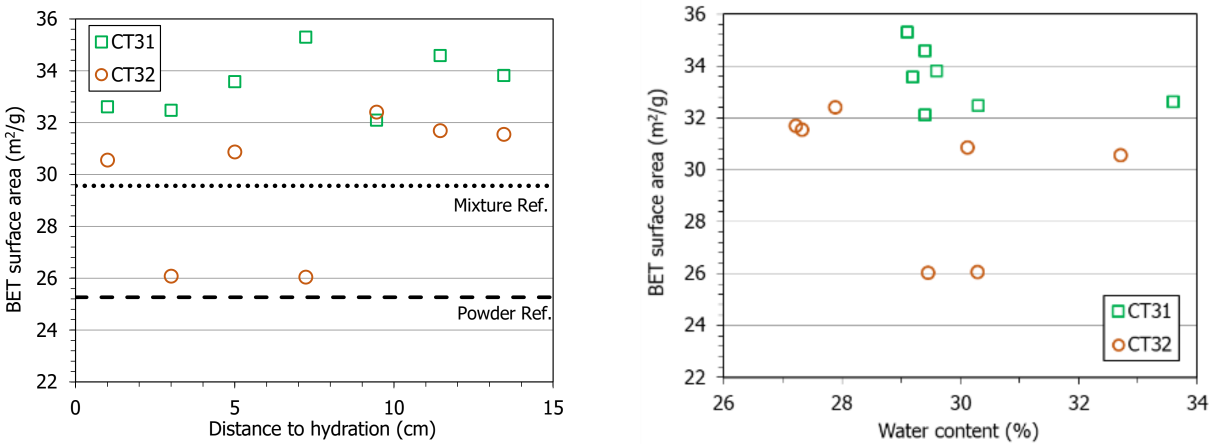

Figure 43. BET specific surface area in subsamples of the two tests as a function of the distance to hydration and the final water content

Figure 44 shows the incremental mercury intrusion curves for samples of the upper and lower halves of the two cells. The void ratio corresponding to pores larger and smaller than 200 nm (e_M and e_m) and the mode size of these two pore families can be inferred from these curves (as explained in subsection 8.2.1) and are shown in Figure 45 and Figure 46, respectively. The hydration process led to changes in the pore size distribution that resulted in an attenuation of the significant initial differences between mixture and block, with the pore size distribution characteristics of both tending to converge. In fact, for a given distance to the heater, the curves corresponding to the two cells were not too different in the upper half of the columns, although they were still different in the lower half:

- In test CT31, the GBM at the bottom of the cell experienced a clear decrease in macropore volume (e_M) and size, tending towards the block values in terms of size (but remaining higher) and decreasing below the initial block value concerning pore volume (but still remaining higher than in cell CT32). However, although the volume of the macropores in samples from the block at the bottom in cell CT32 also decreased with respect to the original block values, their size slightly increased.
- Concerning the family of pores smaller than 200 nm of the samples from the lower half of the cells, its mean size, as far as MIP can explore, did not significantly change, whereas its volume (e_m) increased in the two tests, particularly for the samples of test CT31. However, because e_m for the initial GBM was significantly lower than for the block, it remained considerably higher for the lower-half samples of test CT32 (except for the one at the contact with the hydration surface).

As a result of these changes, particularly those concerning macropores, although the pore size distribution at the bottom of the two cells tended to converge, notable differences still remained. In the samples from the upper halves, e_M was also higher in test CT31, despite the fact that in this area e_M in samples from test CT32 decreased from a value of 2.375, corresponding to the initial GBM. The final e_m in the upper-half samples was similar for the two tests (Figure 45, left), because it considerably increased as a result of hydration in the samples from cell CT32 with respect to the much lower initial GBM value. Hence, because the changes in the GBM were much more important in test CT32 than in CT31, the final pore size distribution in the upper half (where the GBM was placed in test CT32) was more alike for the two cells than in the lower half.

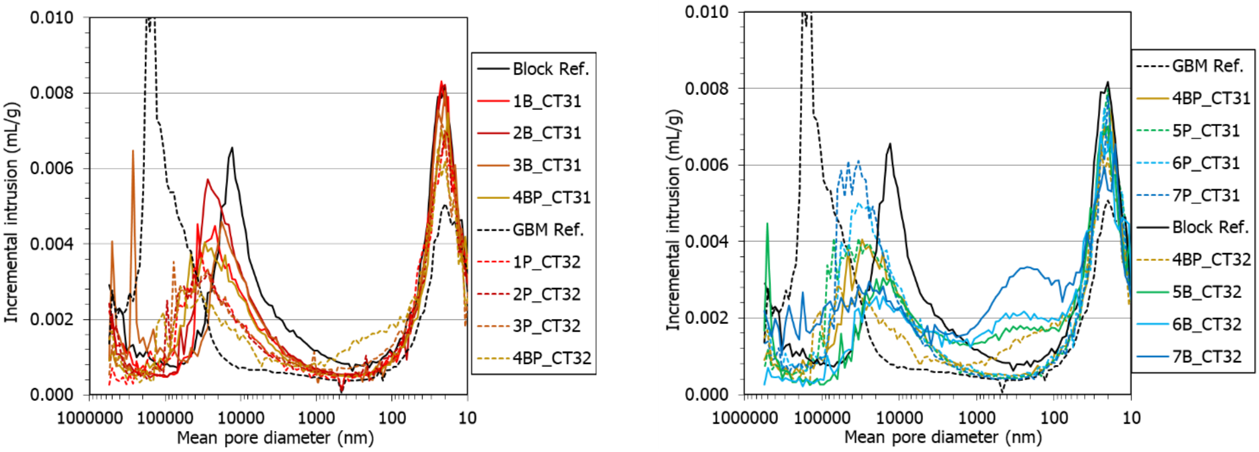

Figure 44. Incremental mercury intrusion as a function of the mean pore diameter in subsamples of the two tests taken from the upper (left) and lower (right) halves of the bentonite column (the y-scale is cut on top and the x-scale on the right to allow better telling curves apart)

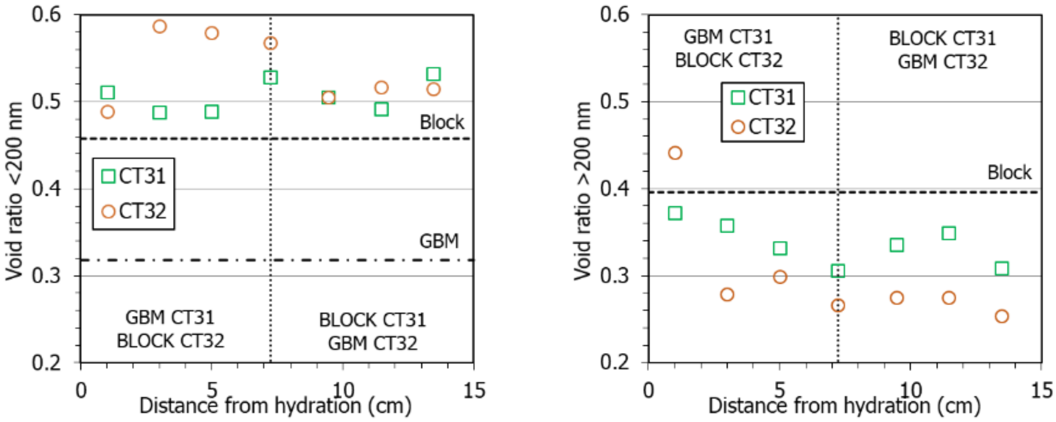

Figure 45. Void ratio corresponding to pores smaller (em, left) and larger (eM, right) than 200 nm of samples of the two tests. The horizontal dashed lines indicate the values for the reference materials (eM in GBM is 2.375, not shown)

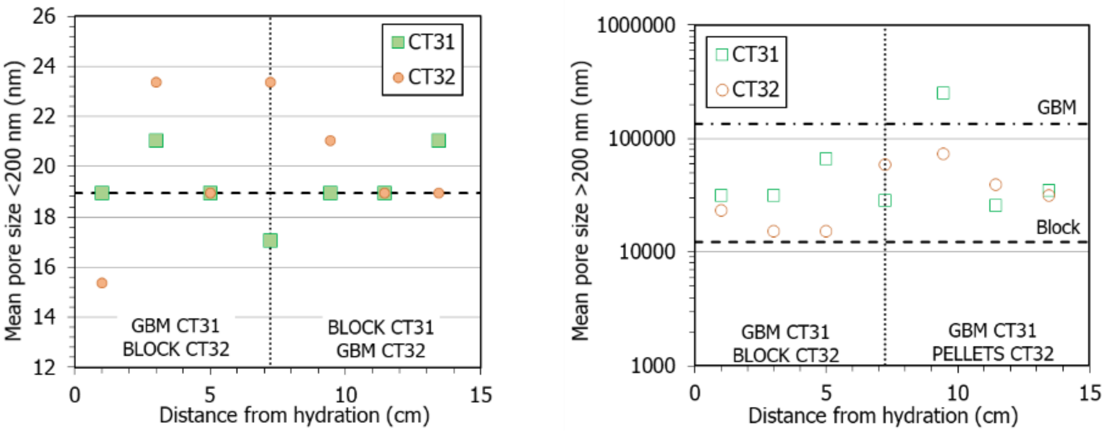

Figure 46. Mean pore size of pores smaller (left) and larger (right) than 200 nm of samples of the two tests. The horizontal dashed lines indicate the values for the reference materials

Hence, MIP showed that there was overall a decrease in the size and volume of macropores and an increase in the volume of pores smaller than 200 nm, which led to a spatially homogeneous increase in the e_m/e_M ratio with respect to the original materials, consistently higher for cell CT32 (Figure 47). Only close to the hydration surface the value for CT32 was lower than for CT31, because of a significant decrease in this area with respect to the rest of the samples from test CT32, triggered by the increase in macropore volume (Figure 45, right), resulting in turn from the density decrease.

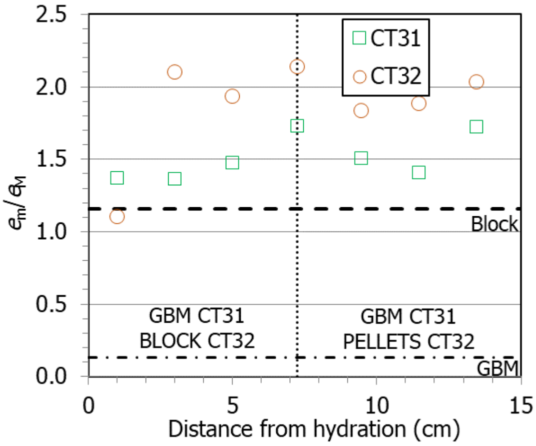

Figure 47. Ratio between void ratio corresponding to pores smaller and larger than 200 nm for the samples from the two cells and for the initial materials (dashed horizontal lines)

The increase in the volume of micropores observed in Figure 45 (left) is likely related to the increase in the smectite basal spacing as a result of the hydration of the interlayer cations. The basal spacing of the MX-80 powder equilibrated at RH=55 % for 48 h is 1.25 nm (Zabala 2025), corresponding to a 1-layer hydration state, which is the usual one for a predominantly sodic bentonite at this RH. This would be approximately the initial basal reflection of the blocks used in the tests, since they were obtained from bentonite equilibrated under hygroscopic conditions. The basal reflection values of the samples at the end of the tests were between 1.58 and 1.47 nm, corresponding in all cases to a predominant 2-layer hydration state (Figure 48). These values were approximately related to water content, increasing with it. In the two cells the maximum value (1.58 nm) was measured in the samples closest to the hydration surface, and for a given distance to this surface, the basal spacing was higher for the samples of cell CT31. In fact, the (001)-reflection of all the samples was a double one that could be decomposed into two diffraction peaks by profile fitting of the XRD patterns (e.g. Figure 28, left). The main diffraction peak corresponding to the full development of the 2-layer hydrate (with values in the range indicated above), and the secondary one, with values generally higher, between 1.60 and 1.79 nm in the samples for cell CT31 and between 1.54 and 1.81 nm for the samples of cell CT32, indicating the transition to the 3-layer hydrate. This secondary peak corresponded to higher basal spacings in the samples from tests CT31 (except for the one closest to the hydration surface and the one at the interface). This would be another indication that the hydration reached in test CT31 was more complete.

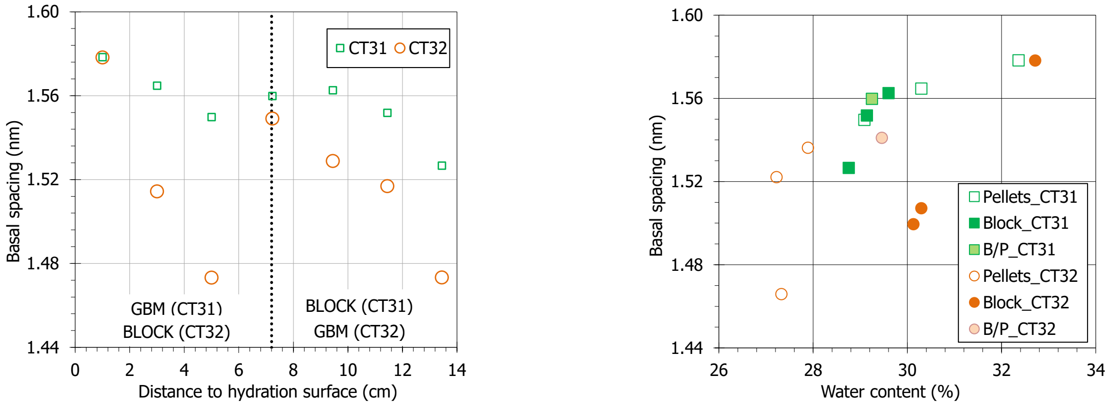

Figure 48. Main diffraction peak of the basal spacing as a function of the distance to the hydration surface (left) and of the final water content of each sample (right) for the two tests

The basal reflection measurements performed in samples of MX-80 bentonite with different water contents and dry densities (Figure 49, Villar et al. 2012 and unpublished results), show that for water contents around 30 %, values of between 1.54 and 1.90 nm can be expected, because this water content corresponds to the transition to the 3-layer hydration state (Villar et al. 2012). Some of the values higher than 1.8 nm shown in the Figure correspond to samples with dry density higher than 1.5 g/cm^3 (Table 4 in Villar et al., 2012). All the samples from the two CT tests had basal spacings in the lower range of those measured in other MX-80 samples (especially those of CT32), despite the fact that their dry densities were only between 1.40 and 1.56 g/cm^3 (Figure 40). So the dry density should not necessarily be a hindrance for having reached the 3-layer hydration state.

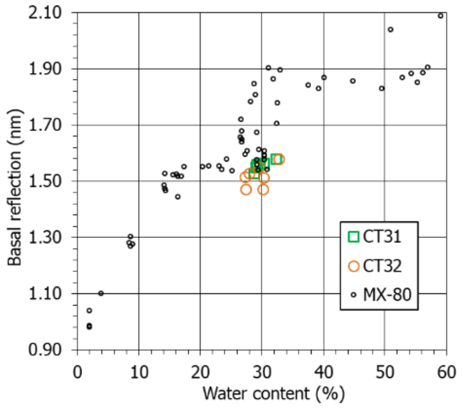

Figure 49. Main diffraction peak of the basal reflection of subsamples of lab tests performed with MX-80 bentonite (values from Villar et al. 2012 and other unpublished results) and of the two tests

In block and GBM samples of FEBEX bentonite saturated under similar conditions as the CT cells, the basal spacings obtained were considerably higher in the GBM part when saturation took place through it and the dry density in the area was lower (Figure 50), with values corresponding even to the fully developed 3-layer hydrate (Villar et al. 2021a). However, in the longest test of this series (MGR28, unreported yet), the dry density along the two-parts bentonite column was homogeneous, and there were no significant differences in the basal spacings of samples from the block or the GBM parts, as it was the case for the CT tests. Hence, water transfer between the smectite interlayer and the bentonite porosity took place in a reversible way during the saturation process of the MGR tests (performed with FEBEX bentonite and a very low initial dry density of the GBM). Perhaps at some intermediate moment during the saturation of the CT cells the basal spacing also corresponded to the 3-layer hydrate. However, no conclusive evidence can be gained in this respect from the analysis of Figure 50, because in the tests with FEBEX bentonite, the dry density in the areas where basal spacings corresponding to the 3-layer hydrate were measured were below 1.4 g/cm^3, whereas the final dry densities in tests CT were always higher than this value.

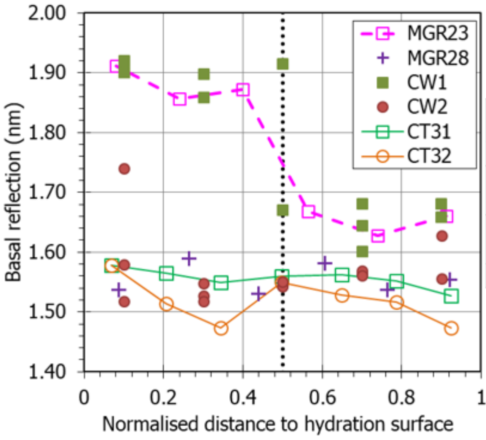

Test	Height	Hydration through	Bentonite	Duration (days)	Dry density (g/cm³)	Degree of saturation (%)
MGR23	10.0	GBM	FEBEX	210	1.43	101
MGR28	10.0	Block	FEBEX	1504	1.45	101
CW1	11.8	GBM	FEBEX	379	1.38	102
CW2	11.8	Block	FEBEX	420	1.39	92
CT31	14.5	GBM	MX-80	922	1.49	100
CT32	14.5	Block	MX-80	844	1.50	99

Figure 50. Main diffraction peak of the basal reflection of subsamples of tests MGR and CW (FEBEX bentonite, length 10 cm in tests MGR and 12 cm in CW, Villar et al. 2021) and CT (MX-80 bentonite, length 14.5 cm). The Table indicates the characteristics of the tests, with final average values for the GBM+block

11 CONCLUSIONS

Some deep geological repository concepts consider as a potential sealing option the use of two-component buffer materials (compacted blocks below the waste canisters and granular bentonite, GBM, filling the rest of the gallery) because they can simplify installation. However, these two components introduce heterogeneities in the system, given its different initial fabric –and sometimes different initial dry density and water content– and consequent evolution during operation. To better understand their behaviour upon saturation, the hydro-mechanical evolution of a two-component bentonite buffer material –a pellet/powder mixture and a compacted block of MX-80 bentonite– was studied by means of two laboratory hydration tests performed under room temperature and isochoric conditions. The GBM mixture consisted of 70 % high-density pellets (2.0 g/cm^3) and 30 % uncompacted powder. The dry densities of the block and the mixture parts were initially the same (1.50 g/cm^3) and the water content similar. The tests were performed in an instrumented cell (15.0x14.5 cm) and hydration with deionised water took place through the bottom of it, under a low water injection pressure. The mixture filled the lower half of the cell in test CT31 and the upper half in test CT32. The rest of the cell was filled with the compacted block, the volume of the two parts being the same. The tests were dismantled after having reached relative humidity and pressure stabilisation and full saturation according to the water intake measurements (922 and 844 days for test CT31 and CT32, respectively).

The analysis of the results obtained allowed to draw the following conclusions:

- As a result of the high initial bentonite suction, the initial water intake was quick in the two cells, even though the water injection pressure was very low. However, because of the large macroporosity of the mixture (where the powder was a low-density preferential pathway occupying 44 % of the initial GBM volume), hydration through the mixture (test CT31) was initially quicker than through the block (test CT32).
- Although the time for full saturation, according to the stabilisation of the water intake, was similar for the two tests, water redistribution inside the bentonite continued afterwards, at least in cell CT31, in which the relative humidity reached 100 % values in the middle and upper part of the bentonite only after stabilisation of the water intake.
- The radial pressure development was not continuous, and was linked to the increase in relative humidity (RH) at every location along the bentonite columns. Close to the hydration surface, the relative humidity increased very quickly to values around 95 %, and subsequently pressure increased steadily and stabilised earlier than at other locations. In

the middle part of the columns, relative humidity started to increase later, and there was a first sharp increase in radial pressure when the water front arrived, followed by an intermediate period of pressure stabilisation (or decrease). Only when the overall degree of saturation was very high (and the RH in the area >95 %), the pressure increased again until its final equilibrium value. This pressure development pattern has been previously observed also in samples of compacted bentonite and of pellets. In the upper part of the cells, pressure did not increase until the RH in the area was higher than 90 %. In test CT32, which had the mixture in the upper half of the cell, a significant collapse took place shortly after the beginning of saturation, reflected in a significant decrease of the radial pressure recorded by the upper sensor.

- The pore pressure build-up on top of the cell was also related to the full saturation of the bentonite in the upper part of the cell, and did not increase up to the stabilisation value until the overall degree of saturation was higher than 97 %.
- The radial pressures measured were exponentially related to the dry density of the bentonite in the area where the sensors were placed. In all cases the pressures measured were higher than what could be expected according to the empirical correlation obtained between axial pressure and dry density from tests in standard oedometers performed with MX-80 bentonite powder compacted at different dry densities. Differences between axial and radial values and the scale effect could explain these higher values in the CT cells.
- Although the initial dry density and water content were the same in the mixture and the block parts, inhomogeneities due to hydration persisted after full saturation and pressure stabilisation, with higher water content and lower dry density in the proximity to the hydration surface. These heterogeneities resulted from the initial swelling and ensuing density decrease of the bentonite that became first saturated (those parts closest to the bottom hydration surface), and the consequent compression of the bentonite located upwards. The shapes of the water content and dry density gradients were not affected by the GBM/block interface, which was barely noticeable to the naked eye. The interface complete healing was checked by injecting gas along it at pressures as high as 4.2 MPa without getting measurable gas flow.
- The hydration process led to changes in the pore size distribution that resulted in an attenuation of the significant initial differences between mixture and block (as detected by mercury intrusion porosimetry), with the pore size distribution characteristics of both tending to converge. The main reason for this homogenisation was a significant reduction in the volume and size of the macropores in the GBM part. The increase of external

specific surface area in all samples points to a disaggregation of clay particles and decrease of their average size, which is consistent with the decrease in the size of the macropores. In both components, GBM and block, there was a substantial increase in the volume of pores smaller than 200 nm and in the basal spacing of the smectite (which is an indication of the number of water layers in the interlayer).

These results provide valuable quantitative and qualitative information about the hydro-mechanical behaviour of two-component buffers, and have shown that their performance during hydration is optimal and that the final state of the two materials tends to homogenise and is essentially similar to that of a one-component buffer.

12 REFERENCES

[1] Åkesson, M., Jacinto, A.C., Gatabin, C., Sanchez M., Ledesma A. 2009. Bentonite THM behaviour at high temperatures: experimental and numerical analysis. Géotechnique 59(4): 307-318. https://doi.org/10.1680/geot.2009.59.4.307

[2] ANDRA 2013. The Cigéo Project – "Meuse/Haute-Marne Reversible Geological Disposal Facility for Radioactive Waste" - Project Owner File Public Debate of 15 May to 15 October 2013.

[3] Bernachy-Barbe, F. 2021. Homogenization of bentonite upon saturation: Density and pressure fields. Applied Clay Science 209: 106122. https://doi.org/10.1016/j.clay.2021.106122

[4] Bernachy-Barbe, F., Conil, N., Guillot, W., Talandier, J. 2020. Observed heterogeneities after hydration of MX-80 bentonite under pellet/powder form. Applied Clay Science 189: 105542. https://doi.org/10.1016/j.clay.2020.105542

[5] Bernachy-Barbe, F., Bosch, J.A., Campos, G., Carbonell, B., Daniels, K.A., Ferrari, A., Graham, C., Guillot, W., Gutiérrez-Álvarez, C., Harrington, J.F., Iglesias, R.J., Kataja, M., Kröhn, K.P., Kröhn, M., Mašín, D., Najser, J., Pingel, J.L., Real, E., Schäfer, T., Svodoba, J., Sun, H., Tanttu, J., Villar, M.V., Wieczorek, K. 2022. Experimental work on bentonite evolution in the frame of BEACON – final report of WP4. BEACON Deliverable D4.3. 237 pp.

[6] Bian, X., Cui, Y.J., Zeng, L.L., Li, X.Z. 2019. Swelling behavior of compacted bentonite with the presence of rock fracture. Engineering Geology 254: 25-33. https://doi.org/10.1016/j.enggeo.2019.04.004

[7] Bosgiraud, J.M., Foin, R. 2016. Test report on FSS metric clayish material emplacement tests with clayish material definition and laboratory work on its performance. Project DOPAS Work Package 3 - Deliverable 3.7. European Commission Grant Agreement no. 323273, 35 pp. https://igdtp.eu/documents/

[8] Brunauer, S., Emmett, P.H., Teller, E. 1938. Adsorption of gases in multimolecular layers. Journal of the American Chemical Society 60: 309–319.

[9] Conil, N., Talandier, J., Noiret, A., Armand, G., Bosrigaud, J.M. 2015. Report on Bentonite Saturation Test (REM). DOPAS Work Package 4 Deliverable D4.2. European Commission Grant Agreement no. 323273, 97 pp. https://igdtp.eu/documents/

[10] Darder, B., Tang, A.M., Pereira, J.M., Dangla, P., Roux, J.N., Chabot, B., Talandier, J., Vu, M.N. 2022. Influence of heterogeneities of density on the hydromechanical behaviour of pellet-based bentonite materials in imbibition experiments. Applied Clay Science 216: 106353. doi:10.1016/j.clay.2021.106353

[11] Dieudonné, A.C., Gatabin, C., Dridi, W., Talandier, J., Collin, F., Charlier, R 2024. Heterogeneous swelling of an isotropically compacted bentonite-based material: Experimental observations and modelling. Rock Mechanics and Rock Engineering 57: 4159–4172. doi:10.1007/s00603-023-03476-z.

[12] Dueck, A., Goudarzi, R., Börgesson, L. 2016. Buffer homogenisation. Status report 3. Technical Report SKB TR-16-04. Svensk Kärnbränslehantering, Stockholm, 104 pp.

[13] ENRESA 2005. Engineered barrier emplacement experiment in Opalinus Clay for the disposal of radioactive waste in underground repositories. Final Report. Publicación Técnica ENRESA 02/05. Madrid, 101 pp.

[14] García-Siñeriz, J.L., Villar, M.V., Rey, M., Palacios, B. 2015. Engineered barrier of bentonite pellets and compacted blocks: state after reaching saturation. Engineering Geology 192: 33–45. https://doi.org/10.1016/j.enggeo.2015.04.002.

[15] Gómez-Espina, R., Villar, M.V. 2016. Time evolution of MX-80 bentonite geochemistry under thermo-hydraulic gradients. Clay Minerals 51(2): 145-160. DOI: 10.1180/claymin.2016.051.2.03

[16] Gutiérrez-Rodrigo, V., Martín, P.L., Villar, M.V., 2021. Effect of interfaces on gas breaktrough pressure in compacted bentonite used as engineered barrier for radioactive waste disposal. Process Safety and Environmental Protection 149: 244–257. DOI: 10.1016/j.psep.2020.10.053.

[17] Harrington, J.F., Daniels, K.A., Wiseall, A.C., Sellin, P., 2020. Bentonite homogenisation within engineered cavities: the evolution of swelling pressure during bentonite hydration. International Journal of Rock Mechanics and Mining Sciences 136, 104535. doi:10.1016/j.ijrmms.2020.104535.

[18] Imbert, C., Villar, M.V. 2006. Hydro-mechanical response of a bentonite pellets/powder mixture upon infiltration. Applied Clay Science 32: 197-209. doi:10.1016/j.clay.2006.01.005

[19] Lee, J.O., Lim, J.G., Kang, I.M., Kwon, S. 2012. Swelling pressures of compacted Ca-bentonite. Engineering Geology 129-130, 20–26. doi:10.1016/j.enggeo.2012.01.005.

[20] Martikainen, J., Pintado, X., Mamunul, H. 2018. Laboratory tests to evaluate bentonite homogenization. Internal memorandum POS-026579. Eurajoki, Finland: Posiva Oy.

[21] Molinero Guerra, A. 2018. Caractérisations expérimentale et numérique du comportement hydro- mécanique d'un matériau hétérogène : mélange de poudre/pellets de bentonite. Ph. Thesis. Université Paris-Est, 190 pp.

[22] Molinero Guerra, A., Cui, Y.-J., Mokni, N., Delage, P., Bornert, M., Aimedieu,Molinero-Guerra, A., Aimedieu, P., Bornert, M., Cui,Y.J., Tang, A.M., Sun, Z., Mokni, N., Delage, P. and Bernier, F. 2018. Analysis of the structural changes of a pellet/powder bentonite mixture upon wetting by X-ray computed microtomography. Applied Clay Science 165: 164-169.

[23] NAGRA 2019. Implementation of the Full-scale Emplacement Experiment at Mont Terri: Design, Construction and preliminary results. NAGRA Technical Report NTB 15-02. Wettingen, 147 pp

[24] Pintado, X., Mamunul, H.M., Martikainen, J. 2013. Thermo-Hydro-Mechanical Tests of Buffer Material. Posiva Report 2012-49. Olkiluoto, 152 pp. ISBN 978-951-652-231-2.

[25] Rawat, A., Baille, W., Tripathy, S. 2019. Swelling behavior of compacted bentonite-sand mixture during water infiltration. Engineering Geology 257: 105141.

[26] Saba, S., Barnichon, J.D., Cui, Y.J., Tang, A.M., Delage, P. 2014. Microstructure and anisotropic swelling behaviour of compacted bentonite/sand mixture. Journal of Rock Mechanics and Geotechnical Engineering 6(2): 126-132.

[27] San Miguel, M. 2022. Análisis de microscopía y micro-tomografía. Informe MI-2022-0007. CENIEH, Burgos, 4 pp.

[28] Sellin, P. 2022. Full project report that includes the synthesis report from the WP1-6. BEACON Deliverable D7.8. 14 pp.

[29] Sposito, G. 1992. Characterization of particle surface charge. In: Buffle J, van Leeuwen (eds.): Environmental particles. Chelsea, MI: Lewis Publ. pp 291 – 314.

[30] Talandier, J. (Ed.) 2019. Synthesis of results from task 5.1. BEACON Deliverable D5.1.2. 334 pp.

[31] Villar, M.V. 2005. MX-80 bentonite. Thermo-hydro-mechanical characterisation performed at CIEMAT in the context of the Prototype Project. Informes Técnicos CIEMAT 1053. CIEMAT, Madrid, 39 pp.

[32] Villar MV, Gómez-Espina R, Gutiérrez-Nebot L, 2012. Basal spacings of compacted bentonite. Applied Clay Science 65-66: 95-105.

[33] Villar M.V., Carbonell, B., Martín, P.L., Gutiérrez-Álvarez, C., Barcala, J.M., 2018. Gas permeability of bentonite samples of the FEBEX Dismantling Project (FEBEX-DP). Informe Técnico CIEMAT 1431. Madrid, 89 pp.

[34] Villar, M.V., Iglesias, R.J., García-Siñeriz, J.L., Lloret, A., Huertas, F. 2020. Physical evolution of a bentonite buffer during 18 years of heating and hydration. Engineering Geology 264: 105408. https://doi.org/10.1016/j.enggeo.2019.105408

[35] Villar, M.V., Iglesias, R.J., Gutiérrez-Álvarez, C., Carbonell, B. 2021a. Pellets/block bentonite barriers: Laboratory study of their evolution upon hydration. Engineering Geology 292: 106272. https://doi.org/10.1016/j.enggeo.2021.106272

[36] Villar, M.V., Carbonell, B., Martín, P.L., Gutiérrez-Álvarez, C. 2021b. The role of interfaces in the bentonite barrier of a nuclear waste repository on gas transport. Engineering Geology 286: 106087. https://doi.org/10.1016/j.enggeo.2021.106087

[37] Villar, M.V., Iglesias, R.J., Gutiérrez-Álvarez, C. 2022. THM column cell with MX-80 pellets simulating the HE-E in situ experiment for 10 years: online results and final physical state. Informes Técnicos CIEMAT 1507. Madrid, 65 pp.

[38] Villar, M.V., Iglesias, R.J., Gutiérrez Álvarez, C. 2024. Saturation of block/pellets barriers of Wyoming bentonite. Informes Técnicos CIEMAT 1542. Madrid, 67 pp. NIPO: 152-24-018-9. ISSN: 2695-8864.

[39] Zabala, A.B. 2025. Estudio de la evolución mineralógica y geoquímica de bentonitas compactadas en experimentos de larga duración en celdas termohidráulicas. Tesis Doctoral. CIEMAT-Universidad Autónoma de Madrid. Madrid, 280 pp.

APPENDIX

VALUES RECORDED BY SENSORS

Table A- I. Relative humidity, temperature and pressure recorded by sensors (sensor "up" placed at 12.8 cm from the bottom porous stone, sensor "mid" at 7.8 cm and sensor "dwn" at 1.3 cm)

Time (days)	RH-up (%)	RH-mid (%)	RH-dwn (%)	*T* (°C)	*P*-up (MPa)	*P*-mid (MPa)	*P*-dwn (MPa)	Pore *P* (MPa)
0	39	40	40	23	-0,01	0,00	0,00	0,094
1	40	40	75	24	0,11	0,11	-0,02	0,108
2	40	40	85	24	0,06	0,10	-0,04	0,111
3	40	40	89	24	0,01	0,14	-0,05	0,113
4	40	41	91	24	-0,04	0,16	-0,05	0,114
5	40	41	93	24	-0,09	0,17	-0,04	0,116
6	40	42	94	24	-0,13	0,19	-0,03	0,117
7	40	42	95	24	-0,18	0,21	-0,01	0,118
8	40	43	96	24	-0,23	0,23	0,01	0,119
9	40	44	97	24	-0,28	0,27	0,05	0,120
10	40	45	97	24	-0,33	0,29	0,08	0,120
12	41	46	98	24	-0,45	0,30	0,14	0,122
14	41	47	98	22	-0,62	0,25	0,22	0,123
16	41	49	99	22	-0,78	0,22	0,29	0,124
18	42	50	99	22	-0,94	0,22	0,35	0,125
20	43	52	99	23	-1,12	0,25	0,40	0,127
22	43	53	100	23	-1,30	0,27	0,45	-
24	44	54	100	23	-1,46	0,35	0,49	-
26	45	56	100	23	-1,60	0,42	0,53	-
28	45	57	100	22	-1,76	0,46	0,57	-
30	46	58	100	22	-1,86	0,55	0,60	-
35	47	61	100	23	-2,15	0,95	0,67	-
40	49	64	100	23	-2,39	1,48	0,73	-
45	50	67	100	23	-2,51	2,09	0,78	-
50	51	69	100	23	-2,45	2,46	0,82	-
55	52	71	100	22	-2,40	2,63	0,87	-
60	53	73	100	21	-2,24	2,71	0,92	-
65	55	75	100	24	-2,02	2,82	0,94	-
70	56	77	100	22	-1,81	3,04	0,98	-
75	57	78	100	22	-1,57	3,24	1,02	-
80	58	79	100	22	-1,32	3,39	1,05	-
85	59	81	100	21	-1,06	3,50	1,08	-
90	60	82	100	22	-0,76	3,57	1,10	-

Time (days)	RH-up (%)	RH-mid (%)	RH-dwn (%)	*T* (°C)	*P*-up (MPa)	*P*-mid (MPa)	*P*-dwn (MPa)	Pore *P* (MPa)
95	61	83	100	21	-0.41	3.62	1.15	-
100	62	84	100	21	-0.08	3.63	1.17	-
110	65	85	100	22	0.37	3.64	1.23	-
120	67	87	100	20	0.72	3.63	1.24	-
130	70	88	100	21	0.85	3.69	1.32	-
140	72	89	100	21	0.96	3.69	1.33	-
150	75	90	100	21	0.98	3.72	1.37	-
160	77	91	100	19	0.97	3.71	1.40	-
170	79	92	100	19	0.92	3.71	1.44	0.154
180	80	93	100	19	0.89	3.69		0.155
190	82	93	100	20	0.87	3.65	1.49	0.156
200	84	94	100	20	0.91	3.64	1.52	0.158
210	85	95	100	20	0.92	3.62	1.57	0.159
220	86	95	100	22	0.95	3.62	1.66	0.162
230	87	95	100	21	1.00	3.60	1.67	0.164
240	89	96	100	22	1.05	3.57	1.66	0.167
250	90	96	100	21	1.09	3.56	-	0.170
260	90	96	100	21	1.15	3.59	1.71	0.172
270	91	97	100	22	1.18	3.58	1.75	0.175
280	92	97	100	22	1.20	3.55	-	0.177
290	92	98	100	21	1.26	3.59	1.83	0.178
300	93	98	100	21	1.29	3.59	1.86	0.180
320	-	98	100	22	1.38	3.61	1.90	0.184
340	-	99	100	23	1.50	3.66	1.94	0.187
360	-	99	100	23	1.60	3.68	2.01	0.188
380	-	100	100	23	1.73	3.74	2.00	0.184
400	-	100	100	23	1.88	3.81	-	0.178
420	-	100	100	21	2.00	3.82	-	0.171
440	-	100	100	22	2.19	3.96	2.20	0.165
460	-	100	100	22	2.38	4.08	2.32	0.158
480	-	100	100	21	2.56	4.17	-	0.150
500	-	100	100	20	2.77	4.31	2.56	0.146
525	-	100	100	20	3.03	4.46	2.75	0.136
550	-	100	100	20	3.40	4.62	2.94	0.121
575	-	100	-	17	3.54	4.56	2.96	0.120
600	-	100	-	22	4.34	5.17	3.27	0.143
625	-	-	-	24	5.00	5.43	-	0.167
650	100	-	-	22	5.28	5.28	-	0.181
675	-	-	-	21	5.72	5.67	3.82	0.192
700	-	-	-	23	5.89	5.31	3.59	0.210
725	-	-	-	16	5.99	5.32	3.73	0.216
750	-	-	-	22	5.94	5.31	3.68	0.218
775	-	-	-	22	6.00	5.25	3.65	0.221
800	-	-	-	24	6.16	5.47	-	0.231
825	-	-	-	21	5.99	5.22	-	0.227
844	-	-	-	21	5.99	5.24	-	0.228

SUBSAMPLING OF SECTIONS

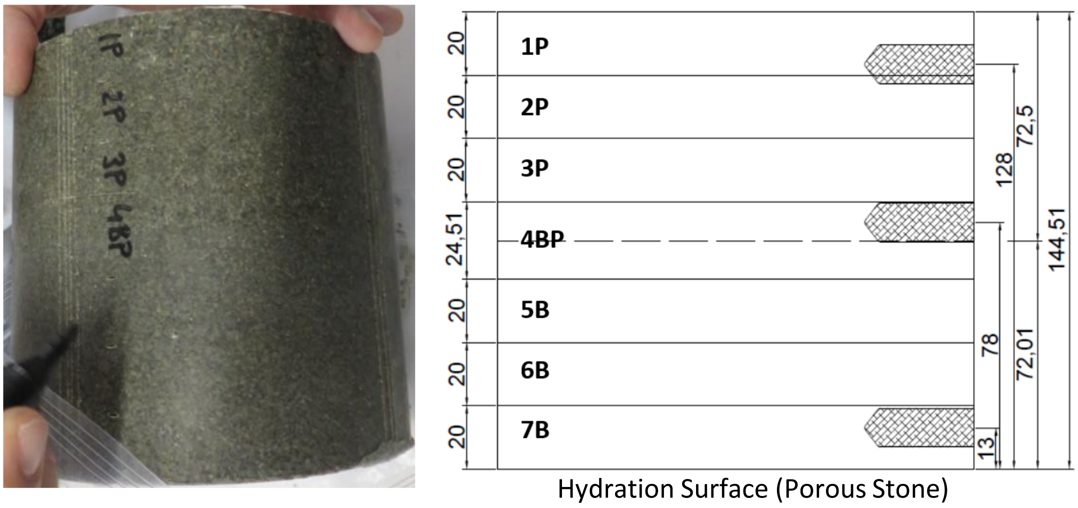

Figure A- 1. State of the sample on dismantling (left) and sampling scheme of the seven sections (right). (B: Block, P: Pellets, dimensions in millimetres)

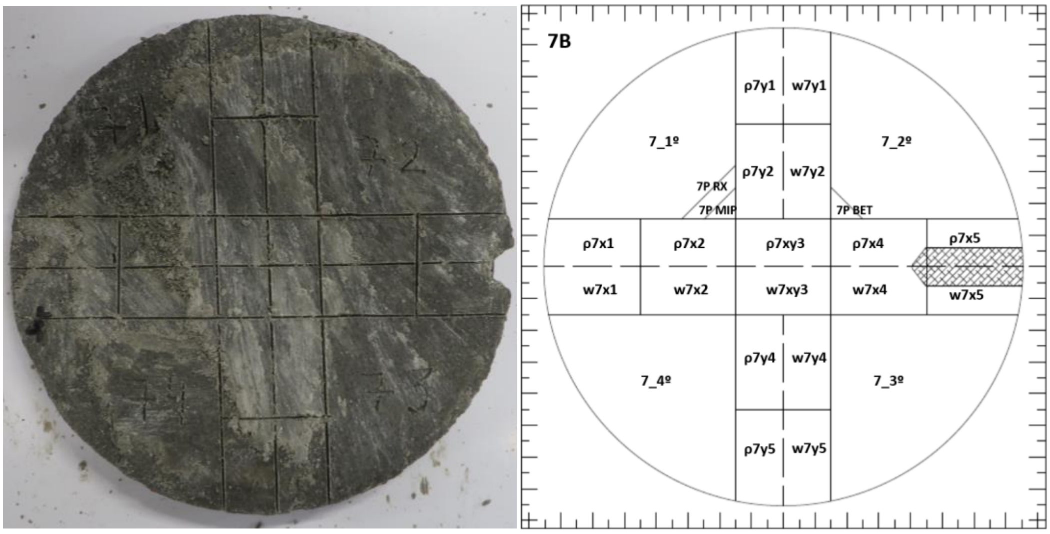

Figure A- 2. Example of a section before subsampling (left) and subsampling scheme in section 7B (right). The X axis is that of the sensors (samples x1 to x5) and the Y axis is perpendicular to it (samples y1 to y5). The kind of determination for each subsample is: w: water content, ρ: dry density, MIP: mercury intrusion porosimetry, BET: BET specific surface area, RX: X-ray diffraction

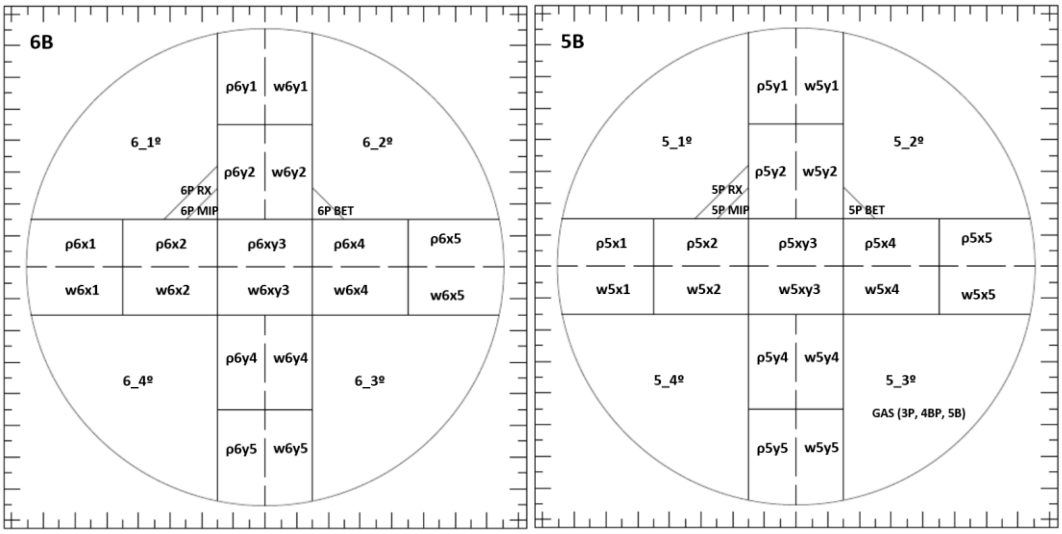

Figure A- 3. Subsampling scheme in sections 6B and 5B

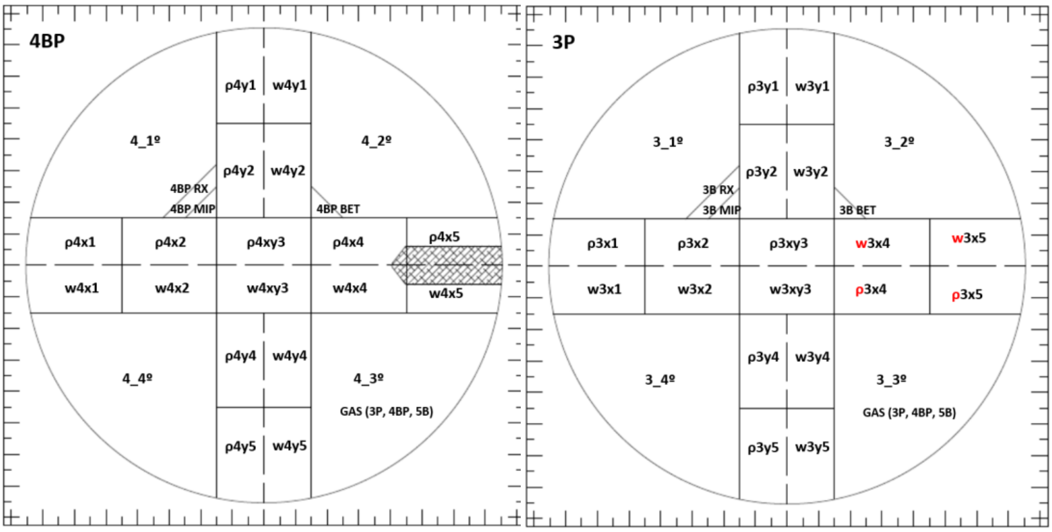

Figure A- 4. Subsampling scheme in sections 4BP and 3P

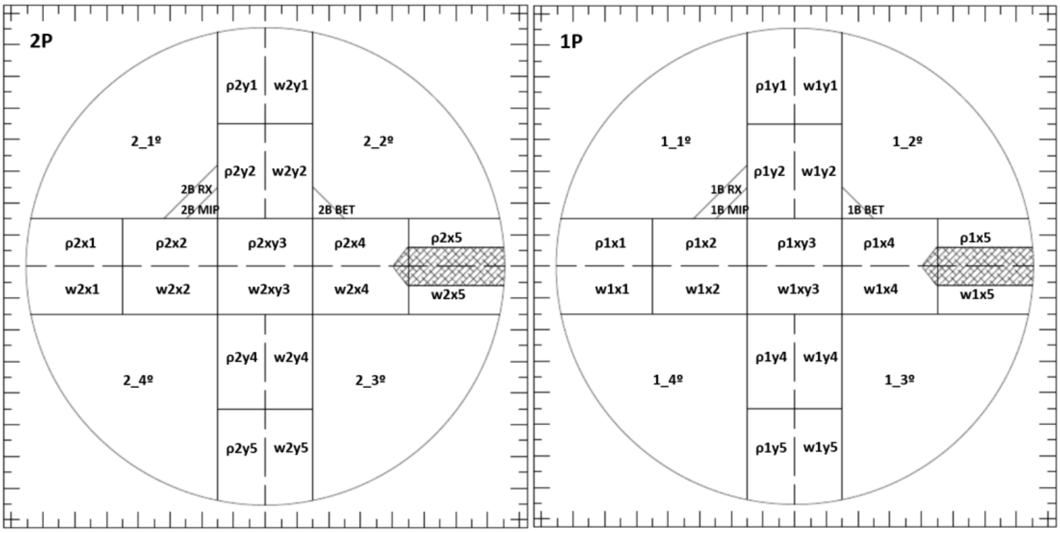

Figure A- 5. Subsampling scheme in sections 2P and 1P

FINAL VALUES

Table A- II. Final water content (w), dry density (ρd) and degree of saturation (Sr) of the subsamples analysed

Reference	Section	Distance to bottom (cm)	Distance to axis (cm)	*w* (%)	ρ_d (g/cm^3)	S_r (%)
7X1	7B	1.00	6.10	33.2	1.42	96
7X5	7B	1.00	6.10	33.9	1.39	94
7Y1	7B	1.00	6.10	33.5	1.42	97
7Y5	7B	1.00	6.10	33.5	1.42	97
7X2	7B	1.00	3.35	32.7	1.44	98
7X4	7B	1.00	3.35	33.1	1.43	97
7Y2	7B	1.00	3.35	32.7	1.43	96
7Y4	7B	1.00	3.35	32.6	1.43	96
7XY3	7B	1.00	0.00	31.9	1.45	96
6X1	6B	3.00	6.10	30.1	1.48	96
6X5	6B	3.00	6.10	30.7	1.47	96
6Y1	6B	3.00	6.10	30.5	1.47	96
6Y5	6B	3.00	6.10	30.3	1.48	96
6X2	6B	3.00	3.35	30.5	1.49	97
6X4	6B	3.00	3.35	30.6	1.49	98
6Y2	6B	3.00	3.35	30.1	1.49	96
6Y4	6B	3.00	3.35	30.4	1.48	97
6XY3	6B	3.00	0.00	30.1	1.49	96
5X1	5B	5.00	6.10	29.9	1.49	96
5X5	5B	5.00	6.10	30.1	1.49	96
5Y1	5B	5.00	6.10	30.5	1.49	98
5Y5	5B	5.00	6.10	30.2	1.49	97
5X2	5B	5.00	3.35	29.9	1.49	95
5X4	5B	5.00	3.35	30.6	1.47	96
5Y2	5B	5.00	3.35	30.4	1.48	96
5Y4	5B	5.00	3.35	30.5	1.48	97
5XY3	5B	5.00	0.00	30.5	1.49	98
4X1	4BP	7.23	6.10	29.0	1.52	97
4X5	4BP	7.23	6.10	30.1	1.48	96
4Y1	4BP	7.23	6.10	29.1	1.53	100

Reference	Section	Distance to bottom (cm)	Distance to axis (cm)	*w* (%)	ρ_d (g/cm^3)	S_r (%)
4Y5	4BP	7.23	6.10	29.6	1.51	98
4X2	4BP	7.23	3.35	29.2	1.51	98
4X4	4BP	7.23	3.35	29.7	1.50	98
4Y2	4BP	7.23	3.35	29.7	1.51	98
4Y4	4BP	7.23	3.35	29.8	1.51	98
4XY3	4BP	7.23	0.00	29.6	1.51	98
3X1	3P	9.45	6.10	27.2	1.55	96
3X5	3P	9.45	6.10	28.3	1.53	97
3Y1	3P	9.45	6.10	27.4	1.55	98
3Y5	3P	9.45	6.10	27.1	1.56	98
3X2	3P	9.45	3.35	27.4	1.55	97
3X4	3P	9.45	3.35	28.4	1.53	97
3Y2	3P	9.45	3.35	28.4	1.54	99
3Y4	3P	9.45	3.35	28.1	1.54	99
3XY3	3P	9.45	0.00	28.1	1.54	98
2X1	2P	11.45	6.10	25.7	1.58	95
2X5	2P	11.45	6.10	27.5	1.55	98
2Y1	2P	11.45	6.10	26.7	1.56	96
2Y5	2P	11.45	6.10	26.9	1.57	98
2X2	2P	11.45	3.35	27.4	1.54	96
2X4	2P	11.45	3.35	27.4	1.54	95
2Y2	2P	11.45	3.35	27.1	1.53	93
2Y4	2P	11.45	3.35	27.7	1.55	99
2XY3	2P	11.45	0.00	27.4	1.57	100
1X1	1P	13.45	6.10	28.2	1.54	99
1X5	1P	13.45	6.10	29.5	1.52	100
1Y1	1P	13.45	6.10	27.5	1.55	97
1Y5	1P	13.45	6.10	27.4	1.55	97
1X2	1P	13.45	3.35	27.4	1.56	98
1X4	1P	13.45	3.35	27.2	1.55	96
1Y2	1P	13.45	3.35	27.3	1.55	97
1Y4	1P	13.45	3.35	27.3	1.56	98
1XY3	1P	13.45	0.00	27.7	1.55	98

CONTOUR PLOTS

2D CONTOUR REPRESENTATIONS OF THE X VERTICAL SECTION

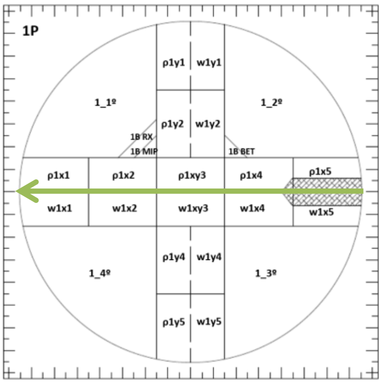

Figure A- 6. The green arrow indicates the position of the vertical cross-section obtained through the X-diameter of the column

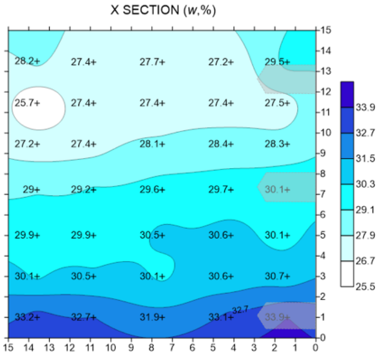

Figure A- 7. 2D contour representation of water content (%) of the vertical section along the X diameter (see Figure A- 6 for location). The shadowed areas indicate the position of the RH/T sensors

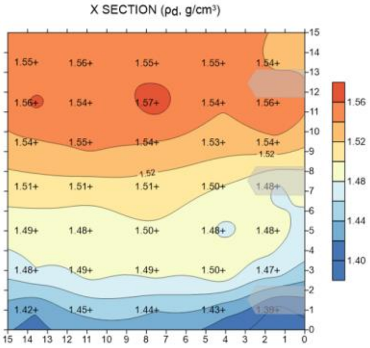

Figure A- 8. 2D contour representation of dry density (g/cm^3) of the vertical section along the X diameter. The shadowed areas indicate the position of the RH/T sensors

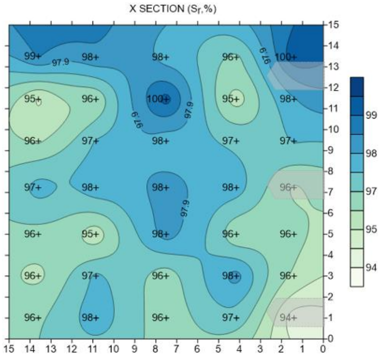

Figure A- 9. 2D contour representation of degree of saturation (%) of the vertical section along the X diameter. The shadowed areas indicate the position of the RH/T sensors

2D CONTOUR REPRESENTATIONS OF THE Y VERTICAL SECTION

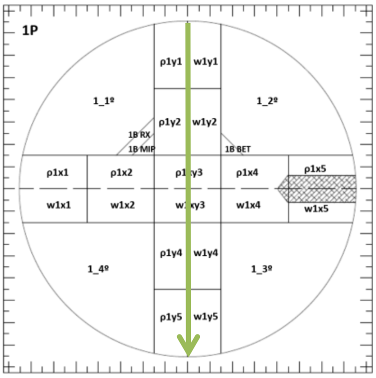

Figure A- 10. The green arrow indicates the position of the vertical cross-section obtained through the Y-diameter of the column

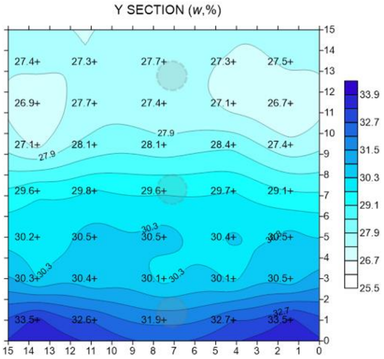

Figure A- 11. 2D contour representation of water content (%) of the vertical section along the Y diameter (see Figure A- 10 for location). The shadowed areas indicate the position of the RH/T sensors

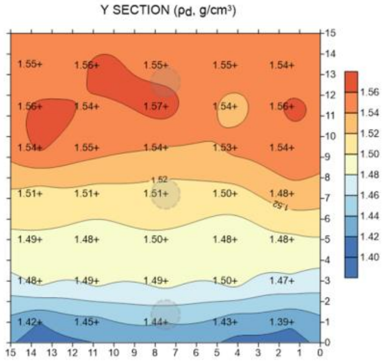

Figure A- 12. 2D contour representation of dry density (g/cm^3) of the vertical section along the Y diameter. The shadowed areas indicate the position of the RH/T sensors

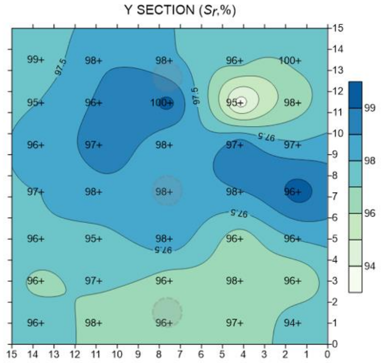

Figure A- 13. 2D contour representation of degree of saturation (%) of the vertical section along the Y diameter. The shadowed areas indicate the position of the RH/T sensors

2D CONTOUR REPRESENTATIONS OF LATERAL DEVELOPMENTS OF THE COLUMN

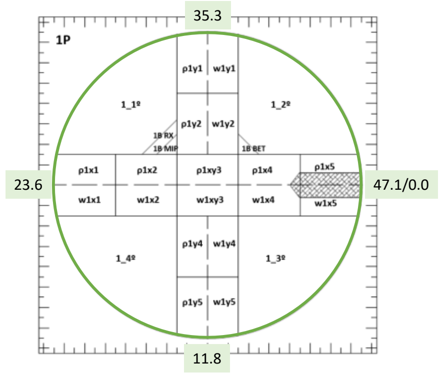

Figure A- 14. The green circle is a cross-section of the surface developed (lateral external surface, with measurements in cm). Highlighted in green: distance in cm for the lateral surface

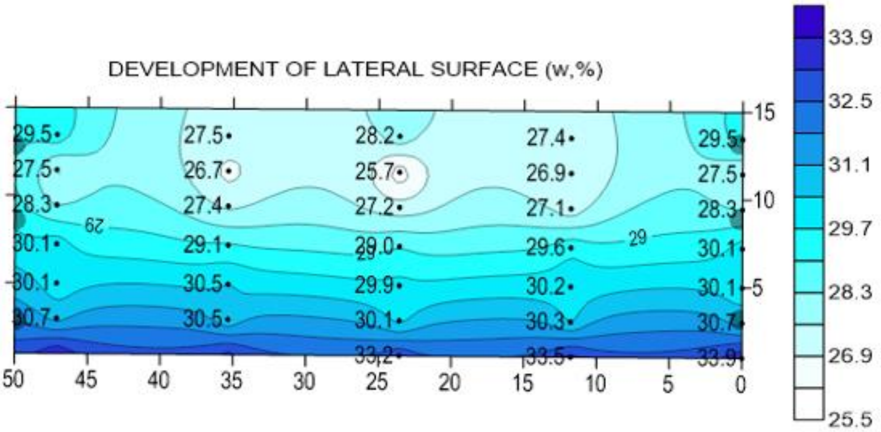

Figure A- 15. 2D contour representation of water content (%) corresponding to the development of the lateral surface of the column. The position of the RH/T sensors is indicated with shadowed semicircles

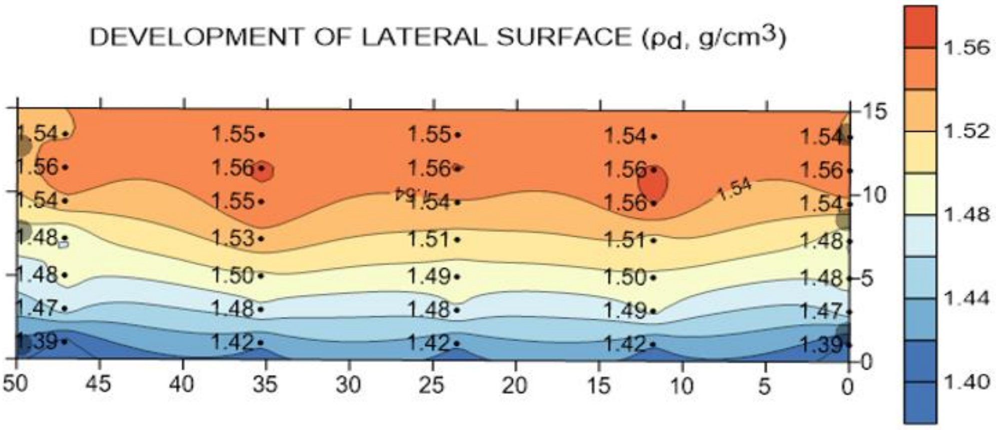

Figure A- 16. 2D contour representation of dry density (g/cm^3) corresponding to the development of the lateral surface of the column. The position of the RH/T sensors is indicated with shadowed semicircles

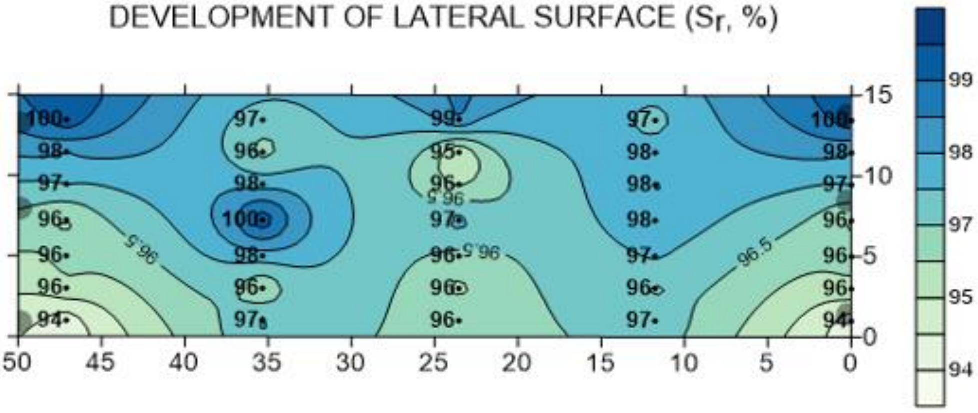

Figure A- 17. 2D contour representation of saturation degree (%) corresponding to the development of the lateral surface of the column. The position of the RH/T sensors is indicated with shadowed semicircles

2D CONTOUR REPRESENTATIONS OF THE INTERMEDIATE DEVELOPMENTS OF THE COLUMN

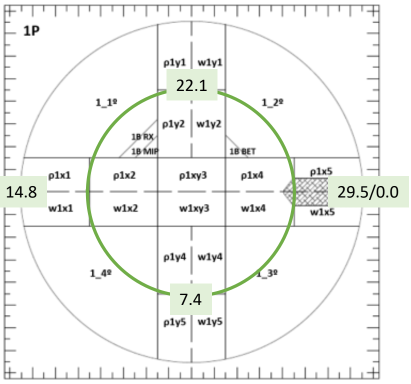

Figure A- 18. The green circle is a cross-section of the surface developed (lateral surface at 4.7 cm from the axis, with measurements in cm). Highlighted in green: distance in cm for the lateral surface

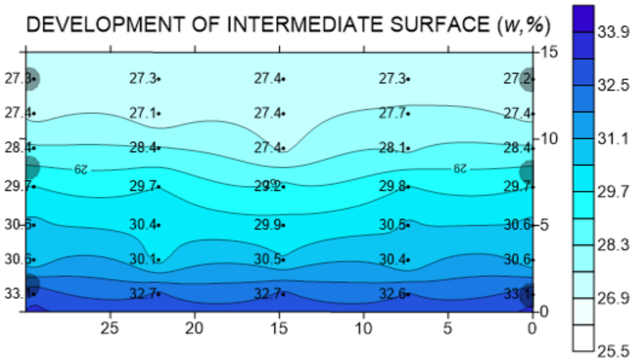

Figure A- 19. 2D contour representation of water content (%) corresponding to the development of the column at 4.7 cm from the axis. The position of the RH/T sensors is indicated with shadowed semicircles

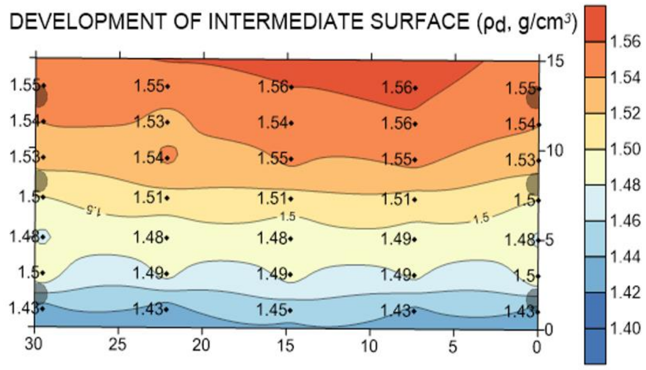

Figure A- 20. 2D contour representation of dry density (g/cm^3) corresponding to the development of the column at 4.7 cm from the axis. The position of the RH/T sensors is indicated with shadowed semicircles

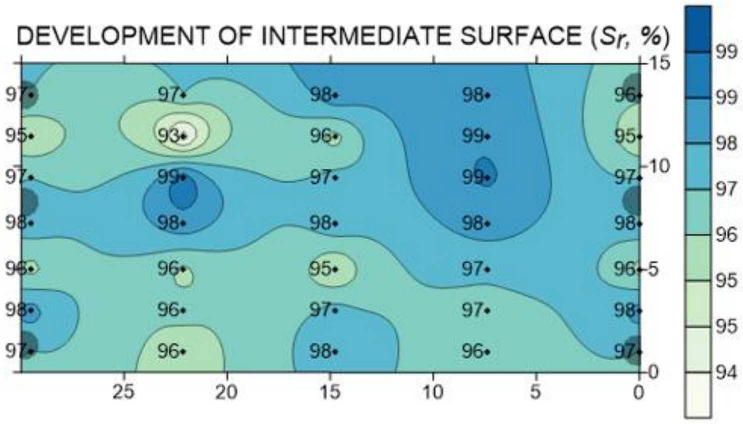

Figure A- 21. 2D contour representation of the degree of saturation (%) corresponding to the development of the column at 4.7 cm from the axis. The position of the RH/T sensors is indicated with shadowed semicircles

2D CONTOUR REPRESENTATIONS OF HORIZONTAL SECTIONS

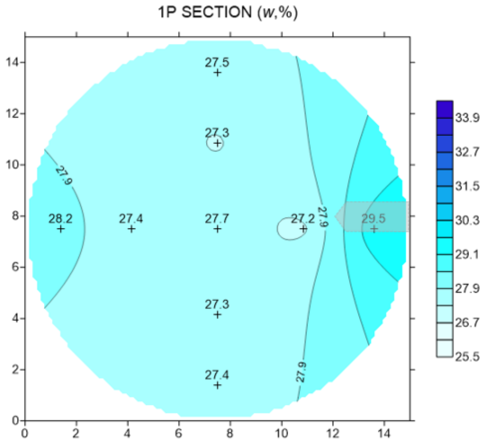

Figure A- 22. 2D contour representation of water content (%) of horizontal section 1P (see Subsampling of sections for location)

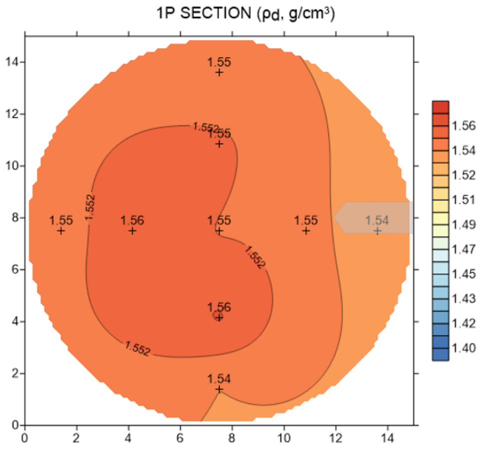

Figure A- 23. 2D contour representation of dry density (g/cm^3) of horizontal section 1P (see Subsampling of sections for location)

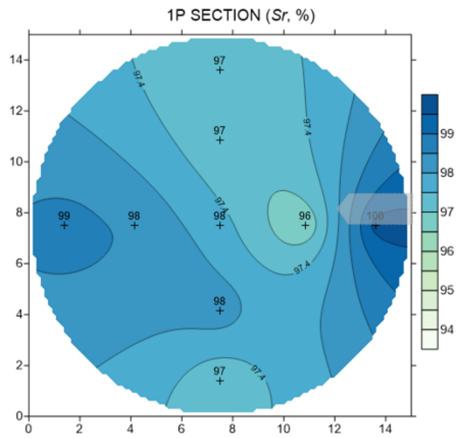

Figure A- 24. 2D contour representation of degree of saturation (%) of horizontal section 1P (see Subsampling of sections for location)

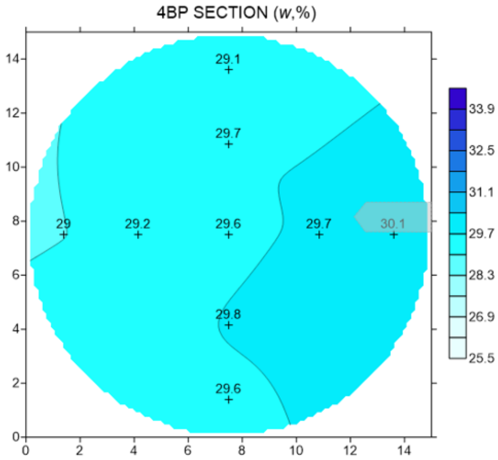

Figure A- 25. 2D contour representation of water content (%) of horizontal section 4BP (see Subsampling of sections for location)

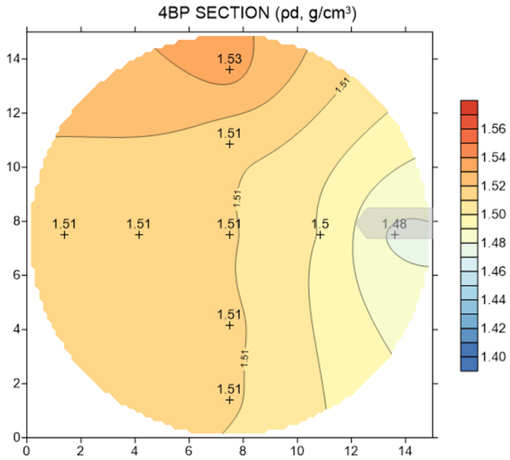

Figure A- 26. 2D contour representation of dry density (g/cm^3) of horizontal section 4BP (see Subsampling of sections for location)

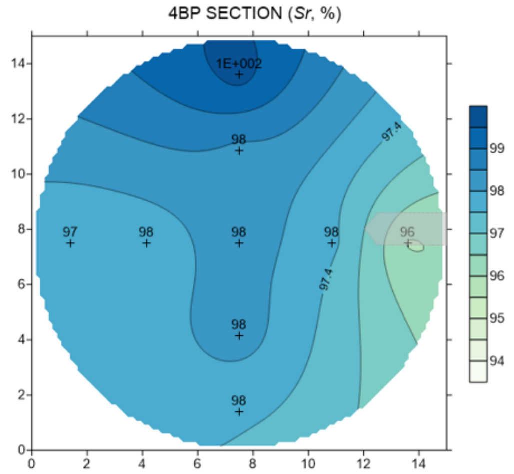

Figure A- 27. 2D contour representation of degree of saturation (%) of horizontal section 4BP (see Subsampling of sections for location)

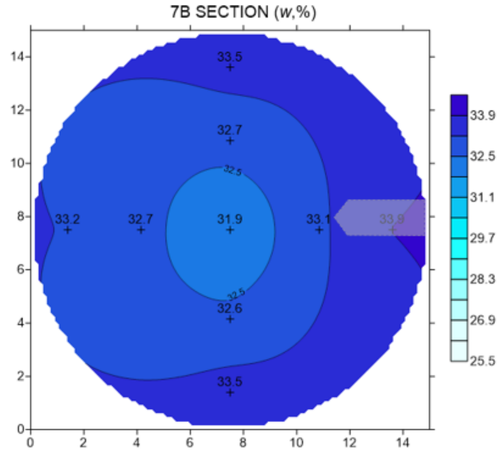

Figure A- 28. 2D contour representation of water content (%) of horizontal section 7B (see Subsampling of sections for location)

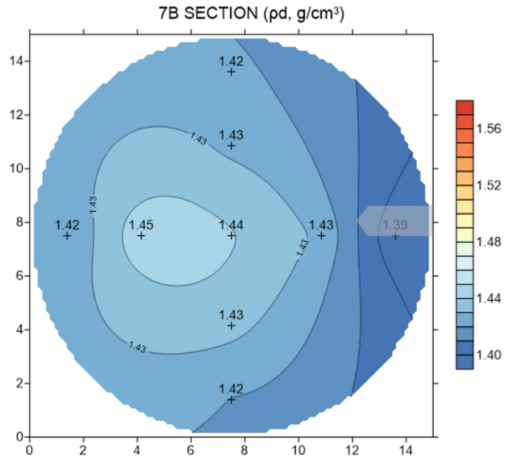

Figure A- 29. 2D contour representation of dry density (g/cm^3) of horizontal section 7P (see Subsampling of sections for location)

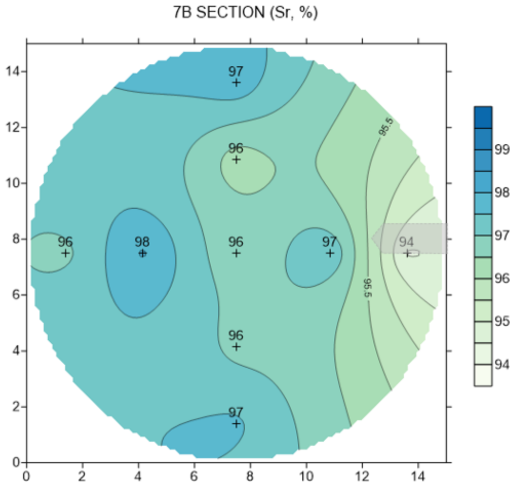

Figure A- 30. 2D contour representation of degree of saturation (%) of horizontal section 7B (see Subsampling of sections for location)

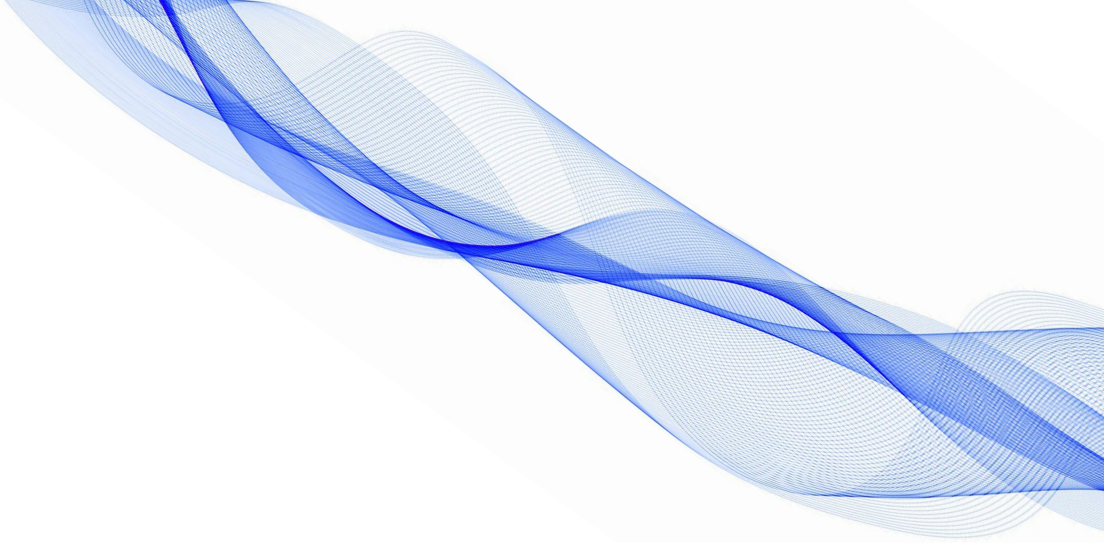

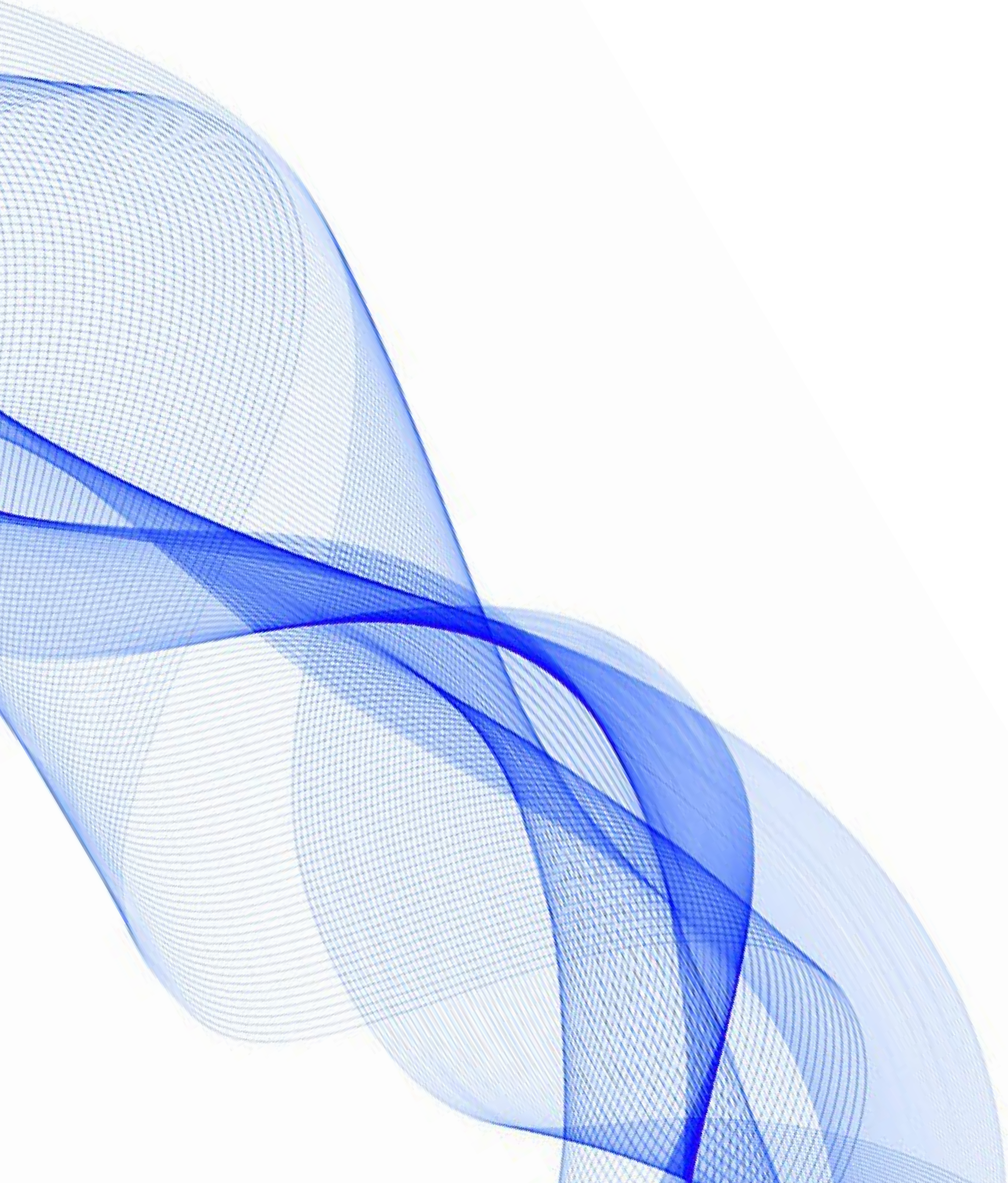

GOBIERNO DE ESPAÑA
MINISTERIO DE CIENCIA, INNOVACIÓN Y UNIVERSIDADES

Ciemat
Centro de Investigaciones Energéticas, Medioambientales y Tecnológicas